



**ESTIMATING EQUATORIAL F-REGION DAYTIME VERTICAL $\vec{E} \times \vec{B}$ DRIFT
VELOCITIES FROM GROUND-BASED MAGNETOMETER MEASUREMENTS
IN THE PHILIPPINE LONGITUDE SECTOR**

THESIS

Shauna M. Kinkela, Civilian

AFIT/GAP/ENP/04-04

**DEPARTMENT OF THE AIR FORCE
AIR UNIVERSITY**

AIR FORCE INSTITUTE OF TECHNOLOGY

Wright-Patterson Air Force Base, Ohio

APPROVED FOR PUBLIC RELEASE; DISTRIBUTION UNLIMITED

The views expressed in this thesis are those of the author and do not reflect the official policy or position of the United States Air Force, Department of Defense, or the United States Government.

AFIT/GAP/ENP/04-04

ESTIMATING EQUATORIAL F-REGION DAYTIME VERTICAL $\vec{E} \times \vec{B}$ DRIFT
VELOCITIES FROM GROUND-BASED MAGNETOMETER MEASUREMENTS
IN THE PHILIPPINE LONGITUDE SECTOR

THESIS

Presented to the Faculty
Department of Engineering Physics
Graduate School of Engineering and Management
Air Force Institute of Technology
Air University
Air Education and Training Command
In Partial Fulfillment of the Requirements for the
Degree of Master of Science (Applied Physics)

Shauna M. Kinkela, BS

Civilian

June 2004

APPROVED FOR PUBLIC RELEASE; DISTRIBUTION UNLIMITED

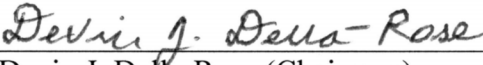
AFIT/GAP/ENP/04-04

ESTIMATING EQUATORIAL F-REGION DAYTIME VERTICAL $\vec{E} \times \vec{B}$ DRIFT
VELOCITIES FROM GROUND-BASED MAGNETOMETER MEASUREMENTS
IN THE PHILIPPINE LONGITUDE SECTOR

Shauna M. Kinkela, BS

Civilian

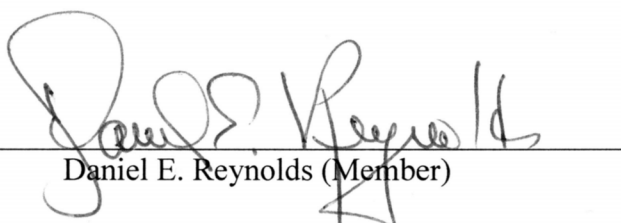
Approved:

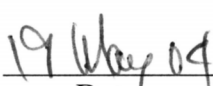

Devin J. Della-Rose (Chairman)


Date


David N. Anderson (Member)


Date


Daniel E. Reynolds (Member)


Date

Abstract

Ionospheric disturbances can severely impact Department of Defense (DoD) systems, such as radar, satellite, and navigation technologies. Forecasting disturbances and describing the Earth's ionosphere, in turn, relies upon innovative computer-based models that gather input parameters from ground and space-borne observations and empirical models for ionospheric drivers. Equatorial $\vec{E} \times \vec{B}$ drift velocities are significant input parameters that go into many ionospheric models, because they help describe vertical plasma motions near the magnetic equator. Previous work by *Anderson, et al* [2002] has demonstrated the ability to derive Peruvian longitude sector, daytime vertical $\vec{E} \times \vec{B}$ drifts from ground-based magnetometer data. The present research extends these results to the Philippines using 56 days of magnetometer data from two stations in 2002.

For each day of magnetometer data, corresponding Global Ultraviolet Imager (GUVI) 1356Å airglow emission data from the evening equatorial anomaly were used to estimate the average $\vec{E} \times \vec{B}$ drift velocities [Anderson, private communication, 2003]. These drift values were then compared statistically to the horizontal component of the Philippine magnetometer data for all 56 days. In this process, data were grouped according to $F_{10.7}$ values. Overall, the best regression relation resulted from the ascending, April 2002 sample of 13 days of data (correlation coefficient of 0.63).

Previous research does not conclusively predict how our April 2002 Philippine slope should compare against the corresponding Peruvian result. Specifically, *Richmond* [1973] predicts the two slopes should be approximately equal. However, *Forbes* [1981] suggests the Philippine regression slope should be 30 percent smaller than the

corresponding Peruvian slope. Our calculated slope difference between the two regression relations is five percent, leaning more toward *Richmond's* prediction.

However, we must keep in mind that our crest separation versus $\vec{E} \times \vec{B}$ relation has a correlation of 0.6, leaving 40 percent of unaccounted variance. Unlike *Anderson's* Peruvian results, no data currently exist to permit validation of our regression relation, yet C/NOFS electric field measurements, when available, may help settle the issue.

AFIT/GAP/ENP/04-04

For Mike

Acknowledgements

I would like to eagerly thank both Dave Anderson and Adela Anghel for their guidance and willingness to help throughout the many stages of my thesis. Besides providing both the data and computer programs used in my research, they each spent a great deal of valuable time answering questions and explaining procedures they used in similar studies. Their kindness, patience, and enthusiasm for the research were crucial for a successful final product.

I would also like to thank Dr. Dan Reynolds for offering his valuable knowledge of mathematics and statistics. His suggestions provided an additional perspective on the research to make it more complete and well-rounded. In addition, Dr. Reynolds' cheerful enthusiasm and support were both encouraging and reassuring.

Most importantly, I would like to thank my thesis advisor, Major Devin Della-Rose, for his consistent and enthusiastic support. Major Della-Rose provided insight, experience, and in many instances a little humor to make my thesis journey a little less "bumpy". His scientific expertise and diligence from beginning to end provided an anchor throughout the entire duration of my thesis. Both the time he spent and assistance he provided are invaluable and will continue to be much appreciated.

One last thank you goes out to my Mom, sister, and brother-in-law for their devotion and support throughout not only my thesis, but my entire graduate education. Without their pride and motivating love, I would not be as successful as I am today.

Shauna M. Kinkela

Table of Contents

	Page
Abstract	iv
Dedication	vi
Acknowledgements	vii
List of Figures	x
List of Tables	xii
I. Introduction	1
Overview	1
Motivation	2
Research Focus and Approach	3
II. Background	7
Overview	7
The Ionosphere	7
Ionospheric Structure	8
The Equatorial Electrojet	10
E-Region Conductivity	11
The Sq Current System and Dynamo Electric Field	13
Formation of the Electrojet	15
The Fountain Effect and Equatorial Anomaly	17
1356 Å Airglow	18
Global Ultraviolet Imager	20
Magnetometers and the H-Component	21
Previous Work in Peru	25
Potential Philippine Results	28
The GAIM Model	31
III. Methodology & Results	34
Overview	34
Choosing Days to Study	34
Viewing GUVI Images	36
GUVI Data Retrieval	40
IDL Code, Input, and Output	41
Determination of Anomaly Crest Separations	43

	Page
Determining the $\vec{E} \times \vec{B}$ Drift Velocity from Anomaly Crest Separations	49
Magnetometer Data Retrieval and Averaging	51
Regression Development	53
Statistics	55
Attempted Validation by Partitioning of Descending Data	58
Division by Month and Season	62
Quiet vs. Disturbed Ascending Days	67
The Final Regression	69
IV. Conclusions and Suggestions for Future Work	71
Appendix A: Derivation of the Limiting Form of the Cowling Conductivity	75
Appendix B: IDL Program Source Code	77
Bibliography	83
Vita	85

List of Figures

	Page
1. Dip Latitude as a Function of Geographic Latitude and Longitude	14
2. Ionospheric Component of the Sq Current During Equinox (1957-1960)	15
3. Diagram of Electric Fields and Current Systems that Contribute to the Equatorial Electrojet	16
4. The Equatorial Fountain Effect	18
5. Earth as Viewed from the Moon in 1356Å Light	20
6. The Local Magnetic Coordinate System	22
7. Latitude Profile for the Daily Range of H (during 1958) with the Component Due to the Equatorial Electrojet Superimposed	23
8. Map Showing the Location of the Magnetometer Site in Muntinlupa, Philippines	24
9. Map Showing the Location of the Magnetometer Site in Davao, Philippines	25
10. Magnitude of the Geomagnetic Field at the Earth's Surface as a Function of Geographic Latitude and Longitude	29
11. GUVI Web Image for Descending Day 282 of 2002	38
12. GUVI Image for Ascending Day 96 of 2002 - Orbit 01773	39
13. GUVI Image for Ascending Day 96 of 2002 - Orbit 01774	39
14. Plot of RadianceT (Rayleighs) versus LatT (°) for Descending Day 282	43
15. Plot of RadianceT (Rayleighs) versus LatT (°) for Ascending Day 96	44
16. Plot of RadianceT (Rayleighs) versus LatT (°) for Descending Day 156	45
17. Plot of RadianceT (Rayleighs) versus LatT (°) for Descending Day 162	46
18. Regression Relation for Average ΔH (nT) versus Inferred $\vec{E} \times \vec{B}$ Drift Velocity (m/s) for All 56 Study Days, Ascending and Descending	53

	Page
19. Regression Relation for Average ΔH (nT) versus Inferred $\vec{E} \times \vec{B}$ Drift Velocity (m/s) for All 43 Descending Days	54
20. Regression Relation for Average ΔH (nT) versus Inferred $\vec{E} \times \vec{B}$ Drift Velocity (m/s) for All 13 Ascending Days	55
21. New Regression for All 56 Study Days (Ascending & Descending) with Points Outside Two Standard Deviations Removed.....	56
22. Average Daily ΔH from Magnetometer Data versus Regression Computed ΔH	60
23. Average Daily ΔH from Magnetometer Data versus Regression Computed ΔH with Regression and Verification Sets Switched.....	61
24. Average ΔH versus Inferred $\vec{E} \times \vec{B}$ Drift Velocity by Month with Points Outside Two Standard Deviations Removed.....	64
25. Average ΔH versus Inferred $\vec{E} \times \vec{B}$ Drift Velocity by Month with Points Outside Two Standard Deviations Removed and 0-Offset.....	65
26. Average ΔH versus Inferred $\vec{E} \times \vec{B}$ Drift Velocity by Season with Points Outside Two Standard Deviations Removed.....	66
27. Average ΔH versus Inferred $\vec{E} \times \vec{B}$ Drift Velocity by Season with Points Outside Two Standard Deviations Removed and 0-Offset.....	67
28. Average ΔH versus Inferred $\vec{E} \times \vec{B}$ Drift Velocity with Quiet and Disturbed Ascending Days Distinguished	69

List of Tables

	Page
1. Anomaly Peak Locations and Crest Separation for All Ascending Days	47
2. Anomaly Peak Locations and Crest Separation for All Descending Days	48
3. Latitude Crest Separation & Inferred $\vec{E} \times \vec{B}$ Drift Velocity (Ascending Days)	49
4. Latitude Crest Separation & Inferred $\vec{E} \times \vec{B}$ Drift Velocity (Descending Days)	50
5. Crest Separation, Inferred Drift Velocity, & Average ΔH (Ascending Days)	51
6. Crest Separation, Inferred Drift Velocity, & Average ΔH (Descending Days)	52
7. Additional (Verification) Descending Day Data Used to Validate the Initial Descending Day Regression Relation	59
8. Initial (Verification) Descending Day Data Used to Validate the Additional Descending Day Regression Relation	61
9. Preliminary, Observed Monthly Mean Values of the Solar $F_{10.7}$ Index for 2002	63
10. Regression Slopes, y-Intercepts, and Correlation Coefficients (R^2) by Monthly Sub-grouping	64
11. Regression Slopes, y-Intercepts, and Correlation Coefficients (R^2) by Seasonal Sub-grouping	66
12. A_p Index, Geomagnetic Conditions, and Regression Data (Ascending Days)	68

ESTIMATING EQUATORIAL F-REGION DAYTIME VERTICAL $\vec{E} \times \vec{B}$ DRIFT VELOCITIES FROM GROUND-BASED MAGNETOMETER MEASUREMENTS IN THE PHILIPPINE LONGITUDE SECTOR

I. Introduction

Overview

As the space weather community learns more about the variation and dynamics of the Earth's ionosphere, it becomes important to develop innovative computer-based models that make use of new advances in space and plasma physics. Ionospheric models rely upon input parameters, based on observations via ground-based and space-borne sensors, in addition to empirical models for primary ionospheric drivers. These input parameters must therefore be as accurate as possible for the model to produce a reliable illustration of the ionosphere. This chapter includes the rationale for maintaining an accurate, real-time, model-based description of the background and disturbed states of the ionosphere, which in turn provides a foundation for forecasting phenomena that can impact Department of Defense (DoD) systems. Also, a summary of the general approach to the research is outlined.

Motivation

The dawning of the Space Age in the late 1950's with the successful launches of Russia's *Sputnik I* and the United States' *Explorer I* gave the world a glimpse into space they had never seen before. With these advancements in technology arose a requirement to understand the space environment and its effects. The science of space weather originated to study space phenomena that not only affected the Earth, but the advancing technologies (e.g. space shuttles, satellites) that the Space Age would introduce.

Since the 1950's, scientists have developed an abundant collection of ground-based and space-borne sensors utilized to describe the space environment. Near real-time measurements and observations from these sensors provide the DoD with a wealth of information related to ion, electron, and neutral densities, plasma dynamics and transport, and chemical production/loss and radiative processes, to name a few. This type of information via ground-based and space-borne sensors, provides scientists with a description of the background state of the space environment, in addition to valuable information concerning space weather storm behavior. Analyzing the data from these sensors helps to produce a limited forecast for the day's activity, but because the condition of the space environment fluctuates depending upon a number of factors (e.g. solar cycle and activity, time, season, and geographic location), forecasting potential space environmental phenomena can become difficult. Some events materialize over time scales of mere minutes and can vanish just as quickly. No matter how instantaneous or lengthy they may be, "disturbances in the space environment (referred to as "space weather") have significantly degraded or eliminated capabilities that all military operations have come to rely upon; GPS, HF and SATCOM, and overhead surveillance,

to name a few [AFSPC/DORW, 1997].” Navigation systems, satellite communications, radars, and many other military systems are vulnerable to space weather stimuli. By exploiting the existence of ground and space-based sensors, scientists must assemble as much intermittent data as possible to produce a workable forecast. Through understanding the underlying science behind these phenomena, computer-based models can be developed to help describe the space environment and most importantly, the behavior and effects of space weather storms. These models therefore become tools that can be used to account for, or correct, DoD systems vulnerable to space weather events.

Research Focus and Approach

State-of-the-art models for describing the space environment assemble various input parameters taken from ground and space-based sensors, then assimilate and correlate these parameters to describe the background and disturbed ionospheric states. The model outputs can then be used by both the operational and scientific communities for application in their respective focus area. For example, the operational advantage becomes the development of forecast products for the effect of the ionosphere on DoD systems.

It becomes a requirement for the input data to be both relevant and accurate, in order for the model to become a useful tool with which we can physically and mathematically describe the upper atmosphere in real-time. In turn, algorithms for determining these input parameters are designed and independently validated, the goal being a complete collection of realistic, up-to-date input data. With this said, this research attempts to derive a longitude specific, empirically-derived algorithm geared

toward calculating the vertical $\vec{E} \times \vec{B}$ drift velocity in the equatorial F-region of the Earth's ionosphere. This drift velocity, in turn, could be a useful, ionospheric model input parameter.

It is known that the vertical $\vec{E} \times \vec{B}$ drift velocity in the equatorial F-region is a result of an eastward daytime electric field, E . The existence of this electric field produces the equatorial electrojet, a daytime current which flows eastward along the magnetic (dip) equator. This current produces a large variation of the magnetic field in the equatorial region [Rishbeth and Garriott, 1969]. Not only does the electrojet produce a variation in magnetic field, its associated eastward electric field leads to a phenomenon, via the vertical $\vec{E} \times \vec{B}$ drift velocity, called the equatorial (Appleton) anomaly. The vertical $\vec{E} \times \vec{B}$ drift velocity lifts plasma to F-region altitudes until diffusion due to pressure gradient and gravity forces cause the plasma to turn around and move down magnetic field lines, away from the equator. The drift and diffusion processes lead to a fountain-like pattern of plasma motion called the equatorial fountain which produces ionization peaks at subtropical latitudes on both sides of the magnetic equator. This phenomenon is the equatorial anomaly [Schunk and Nagy, 2000]. These two resulting effects of the equatorial electrojet and its associated eastward electric field; the variation in magnetic field near the magnetic equator and the ionization peaks of the equatorial anomaly; support a method for inferring the strength of the equatorial, vertical $\vec{E} \times \vec{B}$ drift velocity in the F-region ionosphere.

The motivation for determining this algorithm, specifically applicable to the Philippine longitude sector, comes from a similar study in the Peruvian sector. The

Peruvian study determined the relationship between ΔH , the difference in the parallel component of the geomagnetic field between two magnetometers in the region, and the actual, observed daytime vertical $\vec{E} \times \vec{B}$ drift velocity measured by the Jicamarca Incoherent Scatter Radar (ISR) [Anderson et al, 2002]. Because the Philippine sector does not have an incoherent scatter radar to measure the drift velocities, a preexisting relationship resulting from another Peruvian study was utilized. In the Peruvian sector, a relationship between the latitude crest separation of the equatorial anomaly at ~ 1800 LT and the average, daytime $\vec{E} \times \vec{B}$ drift velocity was established. It is assumed that this relationship is independent of longitude and can be applied to the Philippine sector [Anderson, private communication, 2003]. By examining Global Ultraviolet Imager (GUVI) 1356 Å airglow emission data, the separation of the peaks can be determined and used in the expression to infer an $\vec{E} \times \vec{B}$ drift velocity in a region such as the Philippines, where there is no instrument to make a valid measurement of the quantity. Then, the equatorial variations in the magnetic field strength are considered. The interest is only in the contribution to the Earth's magnetic field resulting from the equatorial electrojet, which can be determined by taking real-time, ground-based magnetometer measurements near the magnetic equator. By using two magnetometer sites, one almost directly on the magnetic equator and another only a few degrees away, measurements can be made for the component of the Earth's magnetic field parallel to the surface. This parallel component is known as the H-component of the magnetic field, and in our case, these measurements will be taken from Philippine magnetometer sites in Davao (7.0 geog. Lat., 125.4 geog. Long., -1.37 geom. Lat.) and Muntinlupa (14.37 geog. Lat., 121.02 geog. Long., 6.26 geom. Lat.). By taking ΔH , the difference in this component between the

two magnetometer sites, we can determine the portion of the Earth's magnetic field resulting only from the ionospheric equatorial electrojet.

The ultimate goal is an empirical relationship between ΔH and the inferred $\vec{E} \times \vec{B}$ drift velocity for the Philippine longitude sector. This relation, if acceptable, could be utilized for input into the GAIM ionospheric model [Schunk et al, 2004]. The GAIM software could automatically assemble the Davao and Muntinlupa magnetometer measurements, apply the data to the algorithm developed in the research, and provide an inferred equatorial, vertical $\vec{E} \times \vec{B}$ drift velocity.

II. Background

Overview

Because the focus of this research is supported in the ionospheric space environment, it is important to understand a few fundamentals of the Earth's ionosphere and the primary phenomena applied throughout the research. Therefore, the equatorial electrojet and equatorial anomaly will be discussed in greater detail, along with a brief description of the types of instruments used to study these phenomena (i.e. GUVI and ground-based magnetometers), what these instruments measure, and how they were important to this research. A discussion of similar studies geared toward using the equatorial electrojet and equatorial anomaly, as a basis for producing an algorithm applicable in the Peruvian longitude sector, is also included. Finally, a summary description of the GAIM model and how the vertical $\vec{E} \times \vec{B}$ drift velocity could be used to establish a GAIM input parameter will be illustrated.

The Ionosphere

The ionosphere is a significant region within the space environment, studied by the space weather community. However, it wasn't until the 1800s that scientists began searching for support of the existence of an ionosphere surrounding the Earth, when Carl Gauss and Balfour Stewart assumed that there must be electric currents present in the atmosphere, creating variations in the geomagnetic field near the Earth's surface. In following years, the ionosphere's existence along with an apparent connection between the Earth's atmosphere and the Sun was often debated. Finally in 1901, G. Marconi

confirmed the existence of the ionosphere with the first trans-Atlantic radio wave transmission. In 1902, A.E. Kennelly and O. Heaviside subsequently suggested that this trans-Atlantic deflection was due to the presence of free electrical charges in the upper atmosphere, and a year later, J.E. Taylor attributed the existence of these charges to solar ultraviolet radiation [Schunk and Nagy, 2000].

As years passed, scientists continued to study the Earth's upper atmosphere. The region was specifically labeled the ionosphere and was defined as the ionized portion of the upper atmosphere. Its altitude extent ranges from 60 to beyond 1000 km and encircles the Earth [Schunk and Nagy, 2000]. The ionosphere is occupied to a large degree by plasma, where electron and ion densities are approximately equal and plasma dynamics are dependent on both local and distant conditions. The primary driver for ionospheric formation is the additional existence of abundant neutrals that can be ionized by solar radiation.

Ionospheric Structure

The Earth's ionosphere is divided into four regions (D, E, F1, and F2) based upon variation in electron density with altitude and the characteristic transport, production/loss, and radiative processes for each altitude range. Because the D- and E- regions are insignificant at night, the four layers can only be distinguished during the day in the mid-latitude region and are usually differentiated by a maximum density at some altitude with a decrease in density with altitude, on each side of the maximum [Schunk and Nagy, 2000].

Distinct ionospheric regions develop because (a) the solar spectrum deposits its energy at various heights depending on the absorption characteristics of the atmosphere, (b) the physics of recombination depends on the atmospheric density (which changes with height), and (c) the composition of the atmosphere changes with height. Thus, the four main ionospheric regions can be associated with different physical processes, rather than simple height differentiation. [Tascione, 1994]

The D-region, the lowest ionospheric region, is located between 60 and about 90 km and relies primarily upon chemical processes. It is composed of positive and negative molecular ions, electrons, and neutral species; of the four layers, it has the highest density of negative ions and neutral species. Because of the altitude of the D-region, water cluster ions dominate and are created via hydration (attachment of water molecules to ions) of the primary ions, NO^+ and O_2^+ . Neutrals, such as N_2 , O_2 , O , and N , in addition to several other minor species, are important for maintaining the D-region [Schunk and Nagy, 2000].

The E-region, from 90-150 km, is also dominated primarily by local chemical processes rather than transport phenomena. With the increase in altitude comes a decrease in neutral density, whereas electron and ion densities are beginning to increase. The dominant ions include NO^+ and O_2^+ , which are governed mainly by photoionization, ion-molecule reactions, and electron-ion recombination [Schunk and Nagy, 2000].

The F-region is usually divided into two separate regions, F1 and F2. A third region, the topside ionosphere (the layer above the F2 peak) is sometimes used to further divide the F-region into three layers. Electron and ion densities continue to increase throughout the F-region, while the neutral density continues to decrease. The F1-region is the lowest, located from 150-200 km. Photochemistry is still dominant in this region;

however there is only one dominant ion, O^+ . Primary reactions include the photoionization of O and loss reactions with N_2 and O_2 . Transport becomes important from 200 km and beyond, which we consider the F2 and topside regions. Plasma drifts due to neutral winds and $\vec{E} \times \vec{B}$ motion, along with ambipolar diffusion are the primary transport phenomena at these altitudes. An F2 peak in the electron density appears at the altitude (usually near 300 km) where the diffusion and chemical processes are equally important [Schunk and Nagy, 2000].

This research will focus primarily on E-region current systems (i.e. equatorial electrojet) and chemistry (i.e. ionization and airglow emission), and F-region transport phenomena (i.e. the fountain effect and equatorial anomaly).

The Equatorial Electrojet

Studies of the Earth's geomagnetic field have shown that even during quiet times, the field experiences noticeable diurnal variations. These variations have been attributed to the solar-quiet (Sq) and lunar (L) systems, which lead to an equatorial, E-region current called the equatorial electrojet. The electric field associated with this electrojet current is the foundation for the vertical $\vec{E} \times \vec{B}$ drift motions that cause the fountain effect and equatorial anomaly. It is therefore important to understand how the electrojet is formed and how it leads to vertical plasma drifts [Schunk and Nagy, 2000].

E-region Conductivity.

The E-region of the Earth's ionosphere is the most conducting of the layers. For this reason, E-region altitudes from 90-120 km range are located in what is commonly called the dynamo region. The critical parameter for determining ionospheric conductivity is Equation (1), the magnetization ratio:

$$\frac{\nu_{jn}}{\omega_j} = \frac{\nu_{jn}}{\frac{|e_j|B}{m_j}} \quad (1)$$

where j can be either ions or electrons.

ν_{jn} = the collision frequency of j with neutrals (1/sec)

ω_j = the gyro frequency of j (radians/sec)

m_j = the mass of j (kg)

$|e_j|$ = the magnitude of the charge of j (Coulombs)

B = the magnitude of the magnetic field (Tesla)

Ions or electrons are considered *magnetized* ($\nu/\omega \ll 1$) when they move without the effects of collisions. When the motion is collision dominated, the particles are *unmagnetized* ($\nu/\omega \gg 1$) and move as if there were no magnetic field present. How magnetized a particle is depends upon both the altitude and the mass of the particle.

At low D-region heights, the high neutral density makes collisions dominant (ν_{jn} large). This forces $\nu/\omega \gg 1$ for ions and electrons, implying that each is strongly unmagnetized and moves parallel to the driving force (e.g. neutral wind or electric field).

When the magnetization ratio, for either particle, approaches 1, the particle is said to be in the transition region, where there are motions both perpendicular and parallel to the driving force. The difference in mass between ions and electrons makes the transition region for electrons at a lower altitude than for ions. For electrons, this transition region is near 75 km while ions do not begin transition until almost 125 km. Near 150 km, the upper bound of the E-region, $v/\omega \ll 1$ for ions and electrons due to the large decrease in neutral density, and the particles are now both magnetized.

As mentioned previously, the E-region dynamo is located between altitudes of 90 and 120 km; where the electrons have already become magnetized and ions have not. Above and below this region, the electrons and ions are either both magnetized or unmagnetized and in both cases move together; an unfavorable condition for the production of currents. Within this region, however, the electrons and ions have relative motions that maximize currents and conductivity. For this reason, the E-region can be considered a highly conducting plasma sheet, sandwiched between the non-conducting D- and F- regions.

There are two important types of currents that flow within the E-region, each of which refers to motion perpendicular to the magnetic field. A Pedersen current occurs when a driving force (e.g. electric field) perpendicular to \vec{B} contributes to a current parallel to that perpendicular driving force. On the other hand, a Hall current occurs when a driving force perpendicular to \vec{B} contributes to a corresponding current perpendicular to both \vec{B} and the driving force. These will be important concepts when

discussing the development of the equatorial electrojet current within the E-region dynamo.

The Sq Current System and Dynamo Electric Field.

The diurnal Sq current system exploits the nature of the E-region to behave like a highly conducting plasma sheet. How this occurs is important when discussing the development of the equatorial electrojet and so is included here.

On the Earth's sunward side, solar radiation heats the thermosphere near the equator causing it to expand. Subsequently, there exists a local high pressure at the equator due to the expansion and a lower pressure toward the northern and southern poles. This pressure gradient leads to neutral thermospheric winds flowing away from the equator, one toward the north pole in the northern hemisphere and another toward the south pole in the southern hemisphere. In turn, the neutral wind tends to drag the ionospheric plasma toward the poles.

The rest of this argument will focus on the northern hemisphere, and be later applied to the southern hemisphere. As stated earlier, we will consider the E-region to be a highly conducting plasma sheet parallel to the Earth's surface. The Sq current system is created thru the effect of Faraday's Law. When applying Faraday's Law, however, we are concerned solely with the \vec{B}_Z (radial) component of the magnetic field; that component perpendicular to the conducting E-region and the Earth's surface.

When the E-region plasma sheet is located above the magnetic (dip) equator, the Earth's magnetic field lines are parallel to the surface, minimizing the \vec{B}_Z component of

the field and the amount of flux passing through the sheet. Figure 1 illustrates the location of the magnetic equator for reference.

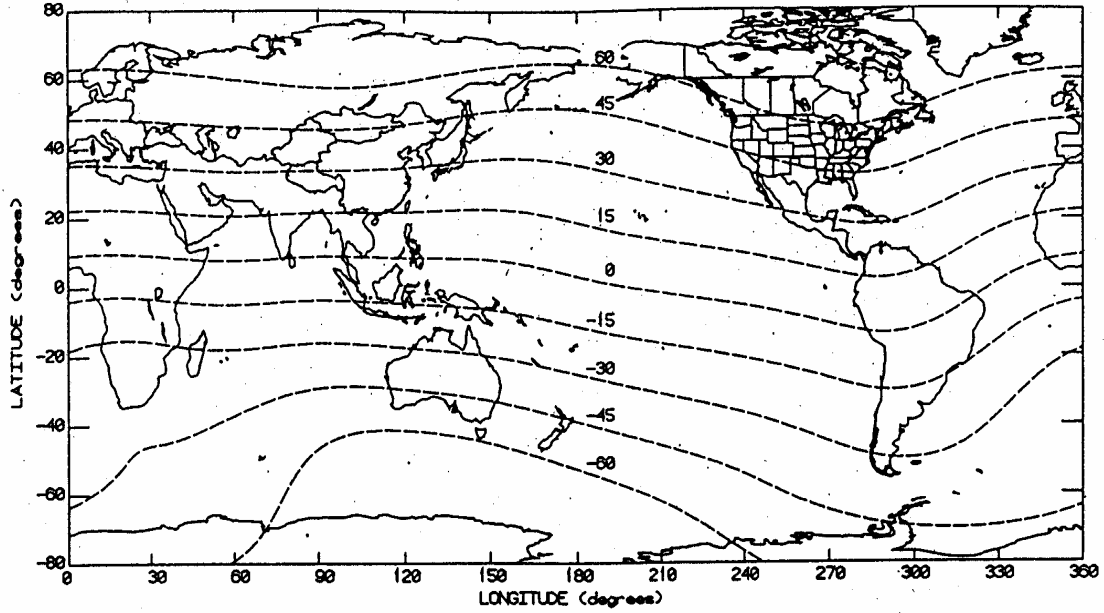


Figure 1. Dip Latitude as a Function of Geographic Latitude and Longitude [West and Heelis, 1996].

However, as the thermospheric wind drags the conducting E-region plasma sheet toward the northern pole, the magnitude of the \vec{B}_Z component and the amount of flux through the sheet increases. As the magnitude of \vec{B}_Z and the flux increases, $\partial \vec{B}_Z / \partial t$ increases and points toward the Earth's surface. When we apply Equation (2), Faraday's Law:

$$\vec{\nabla} \times \vec{E} = -\frac{\partial \vec{B}_Z}{\partial t} \quad (2)$$

a counterclockwise electric field “vortex” is generated in the northern hemisphere. This electric field produces a counterclockwise current flow in the highly conducting E-region.

Near the magnetic equator, the electric field and associated current point in an eastward direction. Figure 2 illustrates this.

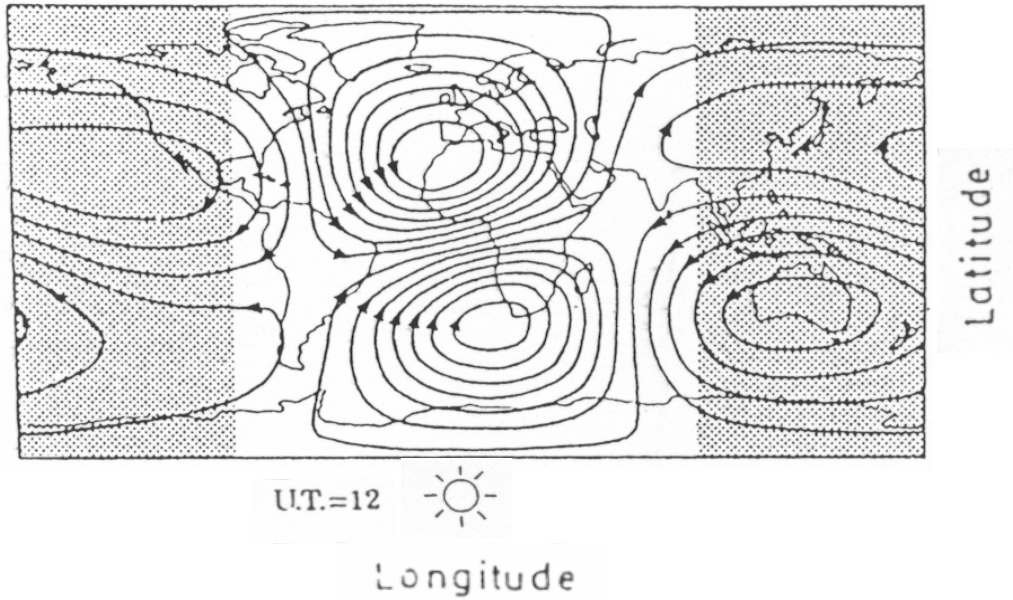


Figure 2. Ionospheric Component of the Sq Current During Equinox (1957-1960) [Volland, 1984].

When this same argument is made relative to the southern hemisphere, the overall electric field flow pattern is clockwise; this also results in an eastward field at the magnetic equator. The resultant eastward electric field in the equatorial E-region is known as the dynamo electric field. On the anti-sunward side of the Earth, a thermal low at the equator reverses the flow direction of both vortices; thus, the electric field reverses direction to flow westward near the magnetic equator.

Formation of the Electrojet.

Within E-region altitudes at the magnetic equator, where magnetic field lines are parallel to the surface and directed northward, this applied dynamo eastward electric field is perpendicular to \vec{B} . Electrons in this region are magnetized and therefore will

experience $\vec{E} \times \vec{B}$ drift motions, whereas the ions are not magnetized. Because of this, the ions must move parallel to any applied force, including the eastward electric field.

The eastward dynamo electric field initially creates an upward $\vec{E} \times \vec{B}$ electron Hall motion within the E-region. It is then important to remember that the E-region is sandwiched between two non-conducting layers. When the upward moving electrons encounter the non-conducting plasma, they build up at the boundary between the regions. The ions, because they are not magnetized, only experience a Pederson motion parallel to the applied eastward electric field. Therefore, there is a resulting charge separation that induces an upward polarization electric field. Figure 3 illustrates this.

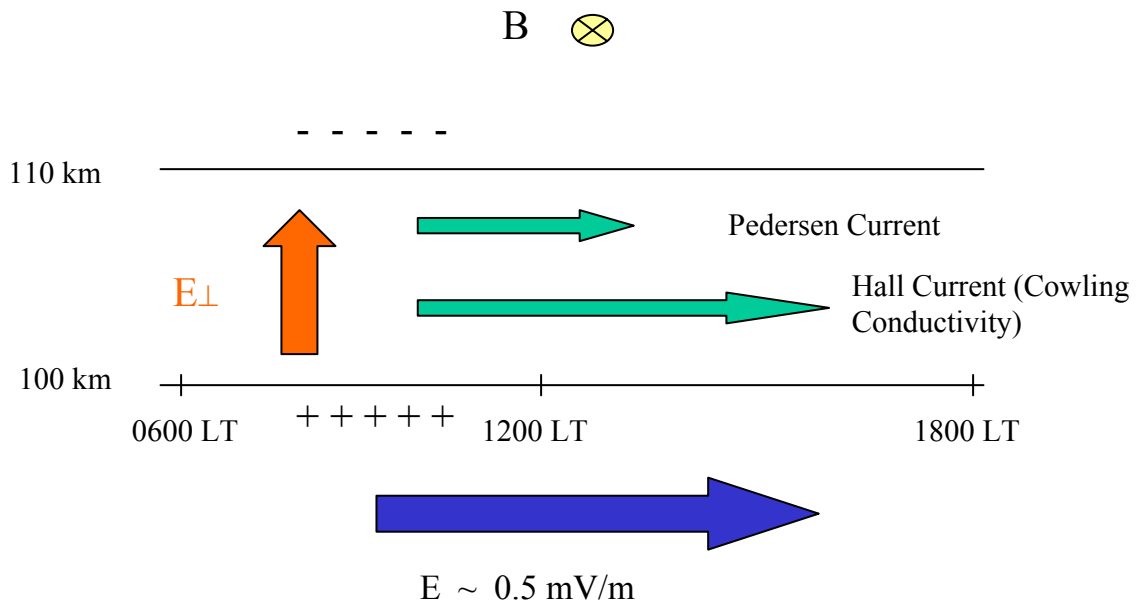


Figure 3. Diagram of Electric Fields and Current Systems that Contribute to the Equatorial Electrojet [Anderson, private communication, 2003].

Outside $\pm 2^\circ$ magnetic latitude, this charge separation cannot be maintained, since there is enough of a vertical component to the magnetic field lines for the built-up charge to drain. Within these bounds, however, the charge separation can be maintained due to the

horizontal nature of the magnetic field near the dip equator. When the induced, polarization electric field is crossed with the northward magnetic field, a “new” westward electron Hall motion results in addition to a corresponding eastward current. Due to an enhanced Cowling conductivity (a combination of Pedersen and Hall conductivities) at the magnetic equator, the eastward ion Pedersen current due to the initial eastward electric field and the eastward electron Hall current due to the charge separation, sum to create a substantial eastward current; this current is the equatorial electrojet.

The Fountain Effect and Equatorial Anomaly.

The eastward electric field during sunlit hours and the geometry of the magnetic field near the dip equator result in an upward $\vec{E} \times \vec{B}$ drift velocity driving magnetized ionospheric electrons to very high F-region altitudes. Within the E-region, the ions aren't magnetized and so cannot move with this $\vec{E} \times \vec{B}$ drift velocity. Yet, the ions are still driven upward with the electrons, due to the magnetic field geometry. Because the magnetic field lines away from the equator pass thru the E-region then arch up into the F-region, the dynamo E-region field in these off-equator regions maps up along the magnetic field into the F-region. At F-region altitudes near the magnetic equator, the magnetic field geometry in addition to the mapped E-region dynamo field produces the fountain effect. As the equatorial plasma rises, it encounters pressure and gravity forces that cause it to diffuse down the magnetic field lines away from the magnetic equator. This fountain-like plasma motion produces a build up of ionization at subtropical latitudes on both sides of the magnetic equator [Kelley, 1989]. This anomaly lasts for the majority of the day, is most prominent near sunset, and fades away after midnight [Rishbeth and Garriott, 1969]. Figure 4 illustrates this process.

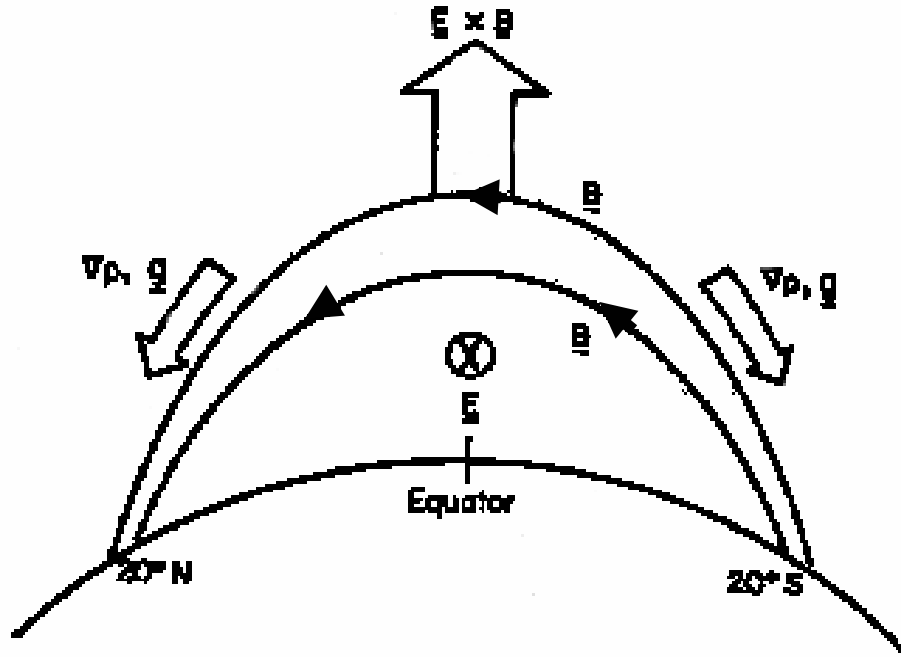


Figure 4. The Equatorial Fountain Effect. The diagram illustrates the fountain-like motion of equatorial plasma and mechanisms that drive the effect. Equator and latitude values are magnetic [Kelley, 1989].

1356Å Airglow

Airglow is energy in the form of visible and UV light, resulting from ionization of the upper atmosphere due to solar UV radiation and energetic particle impacts. On the sunlit side of the Earth, solar photons ionize the upper atmosphere and produce high energy photoelectrons in the Mesosphere and Lower Thermosphere/Ionosphere (MLTI) region. These photoelectrons thermalize, or lose energy, to become thermal electrons. Via radiative recombination, O^+ ions combine with the thermal electrons as shown by the following process [Rees, 1989]:

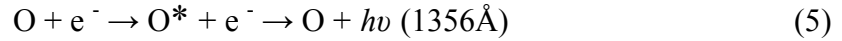


This excited neutral oxygen then de-excites and undergoes the following emission:



The intensity of these emissions is therefore directly related to the density of O^+ and likewise the ambient plasma density.

There are two other processes that result in emissions at 1356\AA ; these being scattered sunlight at 1356\AA and the following neutral oxygen – photoelectron interaction:



However, these processes are not related to the ambient plasma density that we are concerned with; they depend on the neutral and photoelectron densities only and therefore would not provide the necessary information concerning the equatorial anomaly crests. The emissions we are concerned with result from the first process mentioned:

$\text{O}^+ + \text{e}^- \rightarrow \text{O}^* + h\nu$ followed by $\text{O}^* \rightarrow \text{O} + h\nu (1356\text{\AA})$, however, measuring these emissions will only be effective at night. This is because during the day, the intensity of the scattered sunlight at 1356\AA completely overwhelms the emissions due to this airglow. This can be illustrated by Figure 5, on the following page. Measuring 1356\AA emissions away from the auroral zone on the night side, then, is the best method for locating the maximum intensity in airglow emission and corresponding maximum plasma density in the region. The Global Ultraviolet Imager (GUVI) measures emissions at this wavelength, giving us the appropriate data to determine the geographic latitude where these maxima, attributed to the equatorial anomaly peaks, occur.

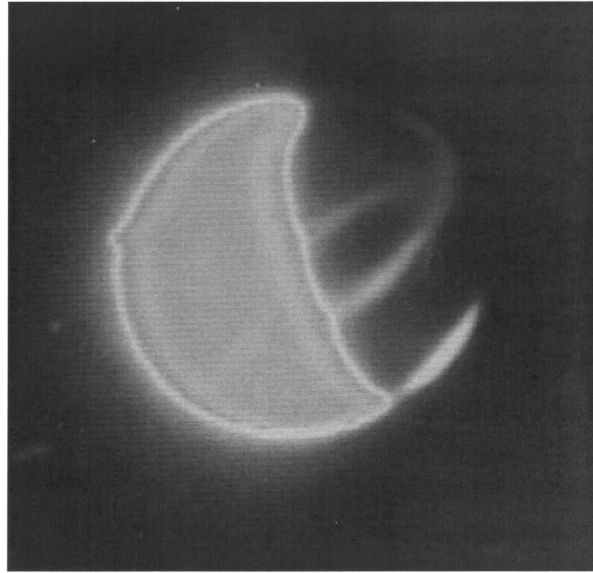


Figure 5. Earth as Viewed from the Moon in 1356Å Light. The night side equatorial anomaly peaks are visible, however on the dayside, these emissions are swamped by scattered sunlight [Anderson, private communication, 2003].

Global Ultraviolet Imager.

Locating the equatorial anomaly ionization peaks requires low and mid-latitude 1356Å airglow data from GUVI, which is an instrument onboard the Thermosphere, Ionosphere, Mesosphere, Energetics and Dynamics (TIMED) satellite. The TIMED satellite, currently in a circular, 625 km polar orbit around the earth, studies the Mesosphere and Lower Thermosphere/Ionosphere (MLTI) region at altitudes between 60 and 180 km [JHUAPL: TIMED, 2003]. It takes about 60 days for the TIMED orbital plane to rotate 180 degrees, or more simply, TIMED covers all local times in about 60 days [Anderson, private communication, 2003].

The TIMED satellite was launched in 2001, providing for available 2002 GUVI data. Initially, the TIMED mission was scheduled to last two years, due to end in the winter of 2004, however, the mission has been extended for three more years of

operations and data analysis to begin in January 2004, with an additional year of data analysis in 2007 after orbital operations have been completed [JHUAPL: TIMED, 2003].

GUVI, one of four instruments on the TIMED spacecraft, is a far-ultraviolet (1150Å to 1800Å), scanning imaging spectrograph that provides data in five wavelength intervals, HI 1216Å, OI 1304Å, OI 1356Å, and the N₂ LBH bands (1400-1500Å and 1650-1800Å). GUVI monitors sources of UV light originating in the MLTI region and maintains a count of individual photons emitted by the upper atmosphere. By globally scanning the MLTI region during each 1½ hour orbit of TIMED, GUVI obtains day (low and mid-latitude), night (low and mid-latitude), and auroral observations, which are used to determine the energy input from the sun into the MLTI region where UV light ionizes atoms and molecules [JHUAPL: GUVI, 2003].

Magnetometers and the H-Component

Because the goal of this research was a relationship between the vertical $\vec{E} \times \vec{B}$ drift velocity and ΔH , the difference in the parallel component of the geomagnetic field between two magnetometers in the Philippine longitude sector, it was important to locate magnetometer sites within the Philippine region that could provide both the necessary data and the optimal location for the research. However, it is important to keep in mind that there is nothing scientifically unique about the Philippine region that motivated the research except the fact that it is located on a landmass with a magnetometer network, along the magnetic equator.

A magnetometer is an instrument measuring variation in the intensity and direction of the Earth's geomagnetic field. These variations can be attributed to electric

currents in the Earth's ionosphere (e.g. the Sq system discussed earlier), and to ring current particles in the magnetosphere. Simply, these magnetometers measure the geomagnetic field via the three components of the local magnetic system; the H-component (horizontal intensity), the D component (declination), and the Z component (vertical intensity). Together, these components give the direction and intensity of the field. Figure 6 illustrates the local magnetic coordinate system.

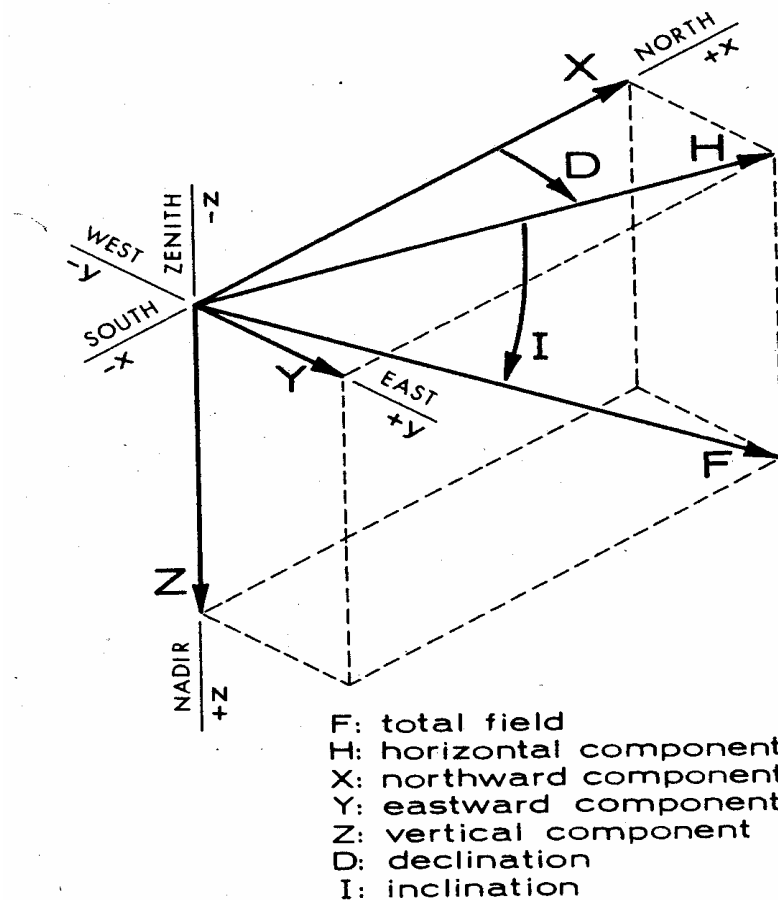


Figure 6. The Local Magnetic Coordinate System [Knecht and Shuman, 1985].

The H-component of the Earth's magnetic field is that component parallel to the surface, but the only portion of this component needed was that which could be attributed to the equatorial electrojet. Figure 7, illustrates the H-component with the electrojet contribution superimposed. When H-component data extracted from a magnetometer a few degrees off of the magnetic equator is subtracted from the H-component value taken from a site almost directly on the magnetic equator, the difference is the H-component related only to the electrojet contribution. This contribution is in turn related to the eastward electric field that created the equatorial electrojet current. By subtracting these values, a ΔH component is determined and the global Sq components and Dst ring current contribution to H are eliminated [Anderson et al, 2002].

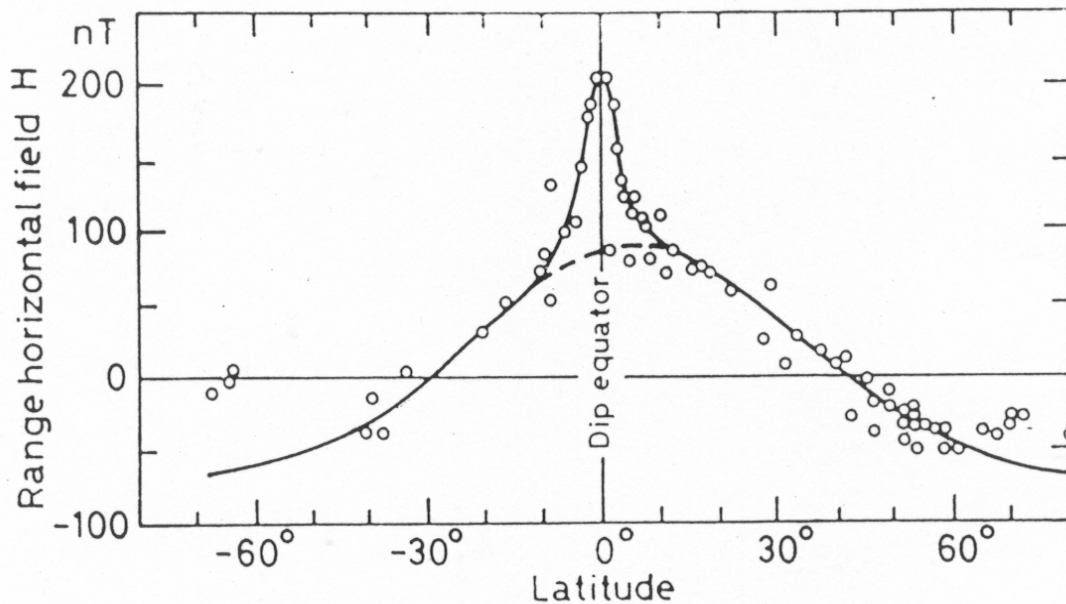


Figure 7. Latitude Profile for the Daily Range of H (during 1958) with the Component Due to the Equatorial Electrojet Superimposed [Rastogi, 1989].

In the Philippine longitude sector, there were two magnetometer sites appropriate for extracting this data. H-component measurements were needed from Philippine magnetometer sites in Davao (7.0 geog. Lat., 125.4 geog. Long., -1.37 geom. Lat.) and Muntinlupa (14.37 geog. Lat., 121.02 geog. Long., 6.26 geom. Lat.). Because of the geomagnetic latitude for these two stations, it was possible to obtain an accurate measure for ΔH , the component resulting from the equatorial electrojet. The following Figures 8 and 9 are maps indicating the locations of these magnetometer sites. Davao and Muntinlupa are stations within the Circum-Pan Pacific Magnetometer Network (CPMN) [Yumoto, 2001; Kyushu University, 2003].

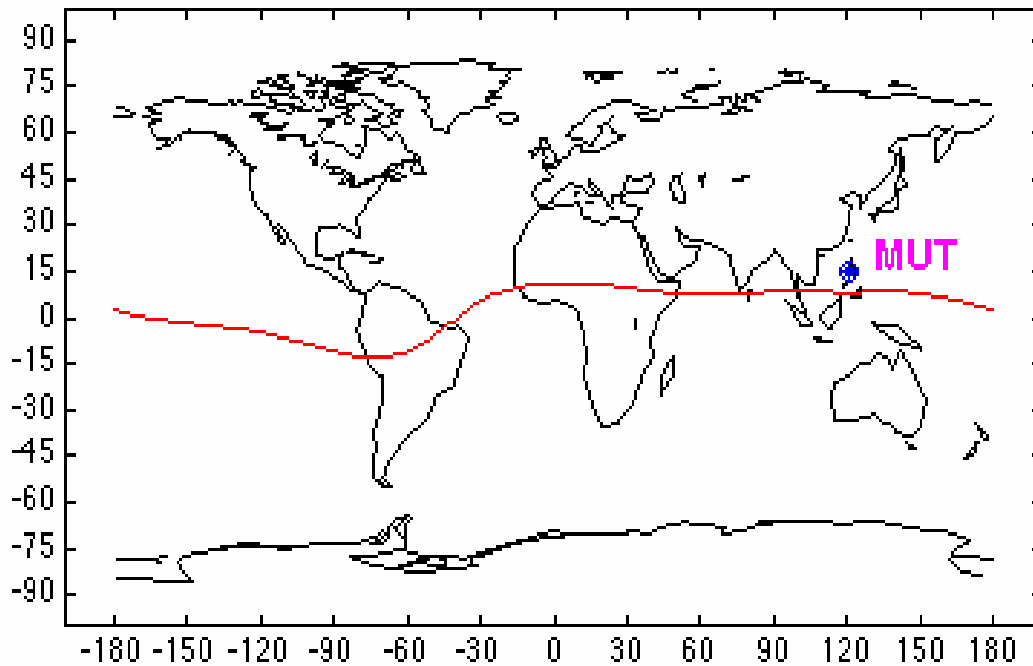


Figure 8. Map Showing the Location of the Magnetometer Site in Muntinlupa, Philippines [Kyushu University, 2003].

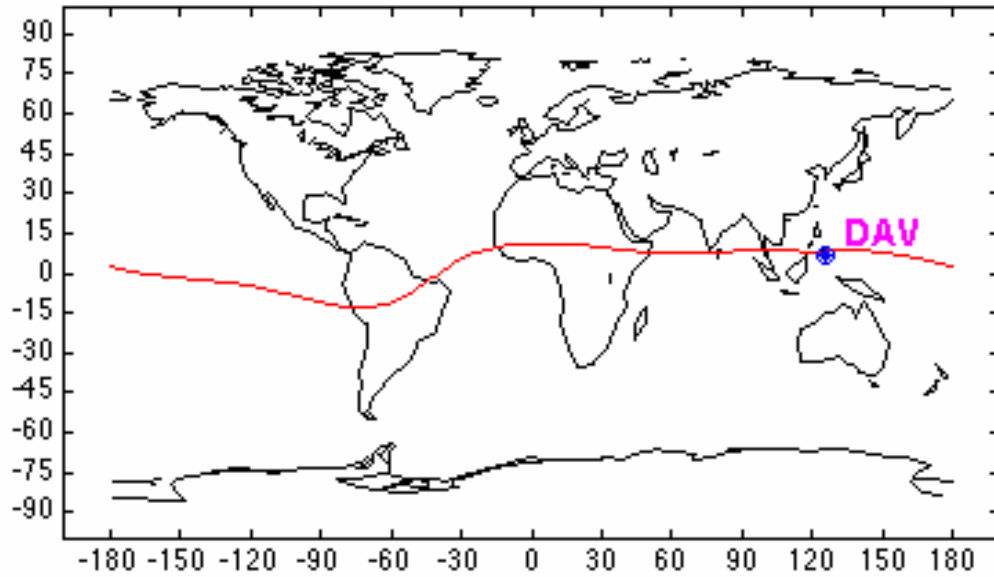


Figure 9. Map Showing the Location of the Magnetometer Site in Davao, Philippines [Kyushu University, 2003].

Previous Work in Peru

This research will make use of two recent studies in the Peruvian longitude sector. These studies were geared toward creating an algorithm for determining the vertical $\vec{E} \times \vec{B}$ drift velocity in the equatorial F-region by relating the drift velocity to ground-based magnetometer measurements in the region.

The purpose of the initial study by *Anderson, et al* [2002] was to produce a relationship between observed, vertical $\vec{E} \times \vec{B}$ drift velocities and the parallel component of the Earth's magnetic field resulting from the equatorial electrojet. Magnetometer readings were taken from two locations in Peru, Canete (-13.06 geog. Lat., -76.38 geog. Long., 0.75 geom. Lat.) and Piura (-5.17 geog. Lat., -80.64 geog. Long., 6.80 geom. Lat.); Canete being located almost directly on the magnetic equator and Piura only marginally displaced. On 10 separate days in 1998 and 1999, magnetometer readings of

H, the parallel component of the geomagnetic field, were taken at each of the two locations. For each of the magnetometer data sets, the nighttime baseline in H was first obtained for each day and then subtracted to give daytime values. This produced daytime H component values with a one minute time resolution. Actual, observed vertical $\vec{E} \times \vec{B}$ drift velocity measurements were then taken from the Jicamarca Incoherent Scatter Radar (ISR) on these 10 days between 1000 and 1300 LT with a five minute time resolution. All of the pairs of ΔH and the corresponding $\vec{E} \times \vec{B}$ drift velocities were then plotted, every five minutes between 1000 and 1300 LT for all 10 days. This resulted in a ΔH versus $\vec{E} \times \vec{B}$ drift velocity plot, which was then analyzed assuming a linear, least-squares relationship. The slope of the straight line was found to be 2.3 nT/m/sec and the off-set was 14.0 nT [Anderson, et al, 2002].

In the initial study by *Anderson et al* [2002], the Jicamarca ISR could provide actual drift velocity measurements. This provided a degree of validity to the Peruvian algorithm because the ΔH versus vertical $\vec{E} \times \vec{B}$ drift relation was based entirely on observed data. However, the Philippine region does not contain an incoherent scatter radar from which to draw actual $\vec{E} \times \vec{B}$ drift velocities. Because there is no ISR in the Philippine sector, our research makes use of an additional study [Anderson and Anghel, private communication, 2003] that provides a method for inferring the average $\vec{E} \times \vec{B}$ drift velocities. As stated earlier, the vertical $\vec{E} \times \vec{B}$ drift velocity in the equatorial region leads to the equatorial anomaly. GUVI 1356Å airglow measurements make it possible to determine the location of the anomaly peaks allowing for calculation of the latitude separation between the peaks. As a result, the following statistical relation between the

anomaly peak separations and the actual $\vec{E} \times \vec{B}$ drift velocities from the Jicamarca ISR, can be used to determine an inferred, average $\vec{E} \times \vec{B}$ value. The R^2 (correlation coefficient) for the following relationship, Equation (6), is 0.5984 [Anderson, private communication, 2003]:

$$\text{Separation (}^\circ\text{)} = 1.05 [\vec{E} \times \vec{B} \text{ Drift (m/s)}] + 17.41(^\circ) \quad (6)$$

This relationship is longitude independent, and can be applied in the Philippine sector, because, to a reasonable approximation, a given numerical value of the $\vec{E} \times \vec{B}$ drift should lead to the same crest separation no matter where the drift occurs along the magnetic equator.

In the Peruvian study, inferred $\vec{E} \times \vec{B}$ values were determined via the GUVI 1356Å airglow data and plotted versus ΔH . The inferred drift velocities could then be compared to actual ISR drift measurements for validation.

The Peruvian relationship relating $\vec{E} \times \vec{B}$ drifts to ΔH can only be applied in the Peruvian longitude sector, which leads to the subject of this thesis; the development of a ΔH versus $\vec{E} \times \vec{B}$ relationship for the Philippine longitude sector. Although the quantitative relationship is not applicable to the Philippine sector, a similar procedure can be used in forming our own relationship. This research will utilize aspects of both Peruvian studies to produce a Philippine ΔH versus $\vec{E} \times \vec{B}$ drift velocity algorithm. In turn, this algorithm could provide a drift velocity that could be used as an input into an ionospheric model.

Potential Philippine Results

It may be possible to theoretically predict what to expect from the Philippine study in comparison to the similar work done in Peru. To do so, however, it is important to know how ΔH relates to B , the magnitude of the magnetic field in the region. The question lies in whether ΔH is proportional to $1/B$ or $1/B^2$.

Scherliess and Fejer [1999] have produced a climatological model of equatorial (vertical) $\vec{E} \times \vec{B}$ drifts for all magnetic longitude sectors. They found that the magnitude of the $\vec{E} \times \vec{B}$ drift (E/B) is basically longitude independent for a given season. Thus, the E/B ratio in Peru and the Philippines should be relatively equal.

An argument can be made to say that ΔH is proportional to $1/B$ using the following reasoning. Assuming that the eastward electric field at the magnetic equator remains equal between sectors, *Richmond* [1973] has shown that a 10% increase in B results in a 10% decrease in H on and off the equator. This would imply that ΔH is proportional to $1/B$. If this is true, on a plot of E/B (x-axis) versus ΔH (y-axis), the slope of a Philippine regression relation should be relatively equal to a corresponding Peruvian slope. At this point, however, it is unclear as to whether this *Richmond* [1973] argument is compatible with the previous *Scherliess and Fejer* [1999] assumption that E/B should be the same in each sector. *Richmond's* [1973] assumption that the eastward electric field is fixed may not allow for both assumptions to hold simultaneously, due to the difference in B between sectors.

Now arguing that ΔH may be proportional $1/B^2$, but maintaining the *Scherliess and Fejer* [1999] result that the magnitude E/B should be equal between sectors, we first

consider that the magnitude of the \vec{B} field between the regions is significantly different.

Figure 10 illustrates this.

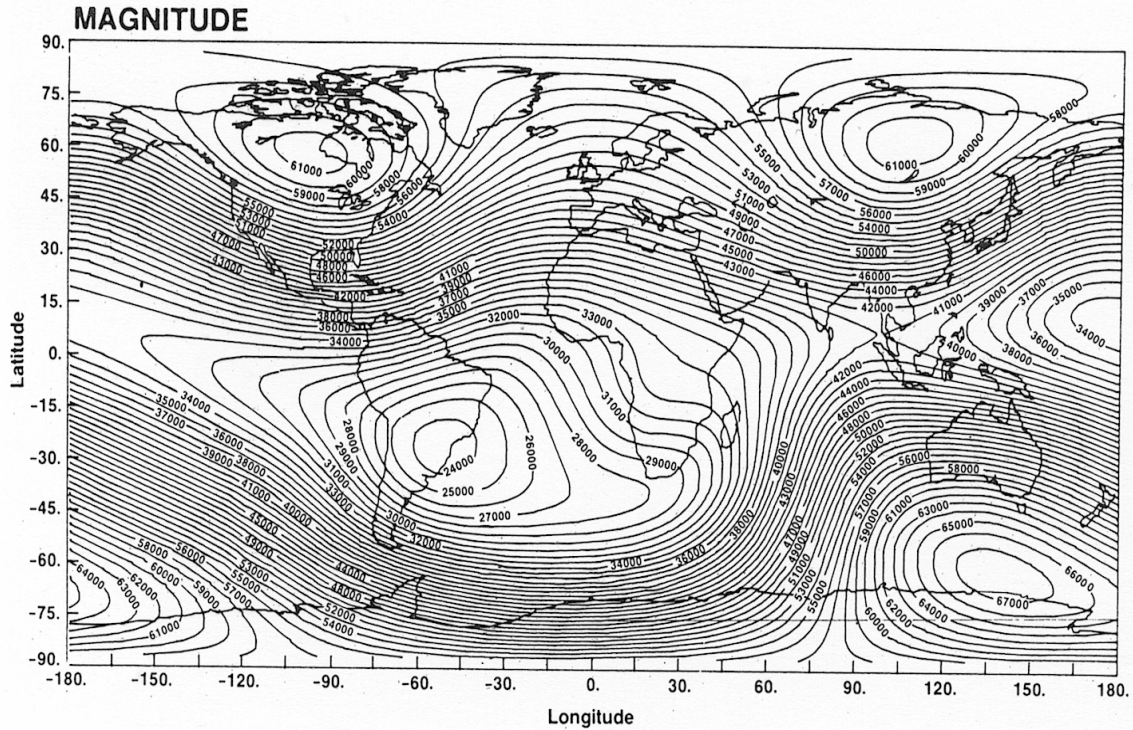


Figure 10. Magnitude of the Geomagnetic Field at the Earth's Surface as a Function of Geographic Latitude and Longitude [Knecht and Shuman, 1985].

We see that near Peru, the geomagnetic field is $\sim 26,000 - 30,000$ nT (0.26-0.3 Gauss).

In the Philippines, however, the field increases to $\sim 40,000 - 42,000$ nT (0.4-0.42 Gauss).

The geomagnetic field in the Philippines is obviously larger, so in order for the magnitude of the $\vec{E} \times \vec{B}$ drift (E/B) to remain relatively equal between the two regions, the dynamo \vec{E} field in the Philippines must also be larger than that in Peru. In addition, assuming the electrojet to be a large, flat current sheet, we can estimate its ground magnetic signature (ΔH), as well as its relation to the dynamo electric field, from:

$$\Delta H \sim \text{electrojet current } \vec{J} \sim \sigma_3 \vec{E}$$

where σ_3 is the Cowling conductivity. ΔH should depend almost exclusively on σ_3 , since its value results from subtracting all influences but the equatorial electrojet.

In general, σ_3 is related to the magnitude of \vec{B} in a complicated fashion via the electron and ion cyclotron frequencies. However, according to *Forbes* [1981], the Cowling conductivity can be simplified in the dynamo region (below 120 km) and still adequately describe electrojet current flow. This limiting form of σ_3 is as follows:

$$\sigma_3 = \frac{m_i v_{in}}{B^2} N_e \quad (7)$$

where σ_3 = the Cowling conductivity (mho/m)

v_{in} = the collision frequency of ions with neutrals (1/sec)

m_i = the mass of the ion (kg)

B = the magnitude of the magnetic field (Tesla)

N_e = the electron concentration (1/m³)

This limiting form was derived for completeness, using assumptions listed in *Forbes* [1981] and *Rishbeth and Garriott* [1969]; see Appendix A for this derivation.

As can be seen by Equation (7), the Cowling conductivity depends upon $1/B^2$, causing ΔH to also depend upon $1/B^2$:

$$\Delta H \sim \text{electrojet current } \vec{J} \sim \sigma_3 \vec{E} \sim \frac{E}{B^2} \sim \frac{E}{B} \bullet \frac{1}{B}$$

Therefore, given that E/B is comparable in both sectors, ΔH would be smaller in the Philippines than in Peru. On a plot of E/B (x-axis) versus ΔH (y-axis), the slope of the Philippine regression relation should thus be smaller than the corresponding Peruvian slope, with the magnitudes of the two slopes differing by about 30 percent, since this is

the approximate difference in B between the two regions. This conclusion would not hold if one encountered individual situations in which E/B varied significantly between Peru and the Philippines. The research may provide support for either this $1/B^2$ argument or that discussed previously; the $1/B$ proportionality argument.

The GAIM Model [Schunk et al, 2004]

Developers of GAIM state that when the model is completed, it will “use a physics-based ionosphere-plasmasphere model as a basis for assimilating a diverse set of real-time (or near real-time) measurements.” GAIM will require real-time input data to forecast the state of the ionosphere on a global, regional, and/or local grid. Making use of ground-based and space-borne sensors such as satellites, ionosondes, magnetometers, and GPS, a wide variety of data will be measured and assembled, along with information concerning solar cycle and activity, season, geographic location, time, and altitude.

A Kalman filter will be used in the model to produce a continuous reconstruction of the global electron density by assimilating the aforementioned data. The use of this filter will efficiently assimilate the different data types while accounting for both model and data uncertainties. Simply, it is a sequential, least-squares procedure for determining the best possible estimate for the state of the ionosphere at some time based upon on all available information.

GAIM is comprised of four levels, or steps. Step 0 of the GAIM system uses the Ionospheric Forecast Model (IFM), based upon both physics-based codes and established empirical models, to provide a time-dependent climatology and the ionospheric specification based on the initial inputs of year, day, start time, duration of run, and the

$F_{10.7}$ and K_p indices. The output is a global N_e distribution from 90-1600 km. This first step runs only when data that support later steps aren't available, making the remaining steps entirely independent of Step 0. Step 1 uses observational data to adjust the empirical IFM drivers to achieve consistency with the measurements. These observationally adjusted models are then run by the Ionosphere-Plasmasphere Model (IPM) and the resulting output, a new global N_e distribution, is an adjusted and improved version of the climatological IFM result from Step 0. Step 2 uses the Step 1 result as an initial guess for a true electron density reconstruction using all of the different data types that pertain to N_e . At this point, the Kalman filter is used to assimilate the data and to combine the IPM results with available real-time measurements, producing a continuous reconstruction of the global N_e distribution from 90-35,000 km. The final step, Step 3, in the GAIM process provides an ionospheric forecast tool for the user. This forecast is produced by using the Kalman N_e specification (Step 2), the adjusted drivers from Step 1, and an existing magnetic index forecast code, to drive an IPM forecast.

The algorithm resulting from this research, if acceptable, could be inserted into the model in Step 1 where observational data are used to adjust the ionospheric drivers. Observations from the magnetometers would be used to estimate the vertical $\vec{E} \times \vec{B}$ drift velocity, and thus the equatorial electric field. These inferred field values would then be used to adjust the Scherliess and Fejer empirical model of equatorial electric fields.

GAIM is very extensive yet remains under development. When the system is completed, it will include both codes and algorithms that must be validated and tested for robustness. Though this research is geared to produce only a single, limited algorithm,

the method used to produce it and its output must be physically accurate for possible integration into the GAIM system. This is what the research will attempt to show.

III. Methodology & Results

Overview

This chapter first provides support as to how and why the studied days were chosen and how the corresponding GUVI 1356Å airglow data and magnetometer measurements were obtained for each day. There is a discussion of the IDL (Interactive Data Language) program, which was used to process and display GUVI data. Editing of the source code for this program, the input, and the output is summarized. Also discussed is use of the IDL output to determine locations for the peaks in ionization resulting from the equatorial anomaly and the corresponding latitude crest separation. Following this will be an explanation of how the average, vertical $\vec{E} \times \vec{B}$ drift velocity was inferred from the crest separation values. Next, the format and daily averaging of the magnetometer data will be discussed. Finally, several average ΔH versus inferred drift velocity regression relations were computed for different groupings of data. The statistics used to improve these relations in addition to validation attempts are mentioned as well.

Choosing Days to Study

The first step of this research was to obtain a set of days to study, with an initial requirement that appropriate GUVI and magnetometer data be available for each day. As stated earlier, these types of data are important for finding the latitude crest separation of the equatorial anomaly peaks and the corresponding average ΔH values on each studied day.

In order for any day's GUVI data to be reliable and appropriate for this study, a TIMED satellite pass had to occur within the Philippine longitude sector and include data in the sunset-to-midnight local time zone. Most of the data fell between 1830 and 2030 LT, but some cases extended slightly outside this range. In the original *Anderson, et al* [2002] study, none of their data went past about 2030 LT. Since the daytime equatorial anomaly exists well into the evening local time sector, the post-sunset GUVI data can be used to characterize this phenomenon. Further, since the daytime $\vec{E} \times \vec{B}$ drift mechanism is the primary shaping force for the anomaly (i.e. effects like the pre-reversal enhancement do not seem to significantly alter the regression results), it is appropriate to compare the GUVI data against the daytime (\sim 0800-1700 LT) magnetometer measurements from Davao and Muntinlupa [Anderson, private communication, 2003].

There are two primary sets of days from 2002 that were suggested [Anderson, private communication, 2003]. On each of the suggested days, the TIMED satellite passed over the Philippine sector and appropriate data was available from GUVI for the required time interval. In addition, the corresponding magnetometer data was available for these days. The following are the initial groupings of the days. They are listed in terms of day of year.

Descending (53 Days):

Initial Group (20 Days): 35, 38, 39, 40, 41, 42, 43, 44, 45, 159, 160, 162, 281, 282, 285, 286, 287, 289, 290, 291

Additional Group (33 Days): 26, 27, 28, 29, 30, 31, 32, 33, 34, 36, 37, 151, 152, 153, 155, 156, 157, 158, 161, 163, 164, 271, 272, 273, 276, 277, 278, 279, 280, 283, 284, 288, 292

Ascending (14 Days): 91, 94, 95, 96, 97, 98, 99, 100, 101, 102, 103, 106, 107, 110

The two main data sets are classified in terms of the type of TIMED polar orbit that passed over the Philippines on that day; “descending” satellite passes or “ascending” satellite passes. A “descending” satellite pass over the Philippines means that the satellite was passing over the region by descending from the northern pole toward the south and an “ascending” pass implies the satellite passed over the region by ascending from the southern pole to the north. The group of “descending” days can be further divided into two sets; an initial group and an additional group. The initial group (provided first by Dr. Anderson) was rather small, so the addition of one more set of days provided both a larger total descending data set and a way to partition the descending data set (later used in validation attempts). After working through some of the research, several days were excluded from the study. The reasoning behind these exclusions will be discussed later in the chapter.

Viewing GUVI Images

The first step of the research was to examine GUVI images for each of the suggested days, in order to begin determining the latitude crest separation of the anomaly peaks. Images of these satellite passes could be viewed at an online source devoted to the instrument. Visiting this site, <http://guvi.jhuapl.edu/gallery/gallery/gallery.cgi>, was necessary in order to determine the exact orbit(s) of the TIMED satellite that passed over the Philippines, so that the data for the pass could be obtained at a later time. The following step-by-step process was used to obtain a TIMED orbit number(s) for each of the 67 days (listed previously).

1. On <http://guvi.jhuapl.edu/gallery/gallery/gallery.cgi>, I chose Level 1B Survey - Product Gallery
2. Under "Day", I chose the day I wanted to view. The choices are listed in the following format: YEAR-DOY where DOY refers to the day of year.
3. Under "Data Views" I chose "Descending (or Ascending) Equator", which implies a descending (or ascending) overpass by the TIMED satellite and an image centered in the equatorial region.
4. Under "Wavelengths" I chose 1356 referring to 1356Å emissions.
5. I chose "Retrieve Image" to open the image for the first orbit on that day. However, this image usually did not show a satellite pass over the Philippine region.
6. Therefore, I chose "Next Orbit" to cycle through each longitude for the chosen day. This was done in order to find the satellite orbit that did pass over the Philippines for that day.

[Anghel, private communication, 2003]

After completing this process, a web page with an image was present; an example of the resulting web page appears in Figure 11, on the following page. As can be seen by this figure, the web page provides a great deal of information, including the start and end times for the orbit and the filename corresponding to the GUVI data that created the image. In the example case of Descending Day 282 (Figure 11), the orbit number is 04528 and the corresponding filename is:

GUVI_im_disk_v008r00_2002282_REV04528.L1B

For each descending day, only one orbit over the Philippines contained all important information (i.e. maximum radiances and locations for *both* anomaly peaks). However, in the ascending orbit cases, instrumentation and TIMED orbit characteristics force this information to be divided into two orbits.

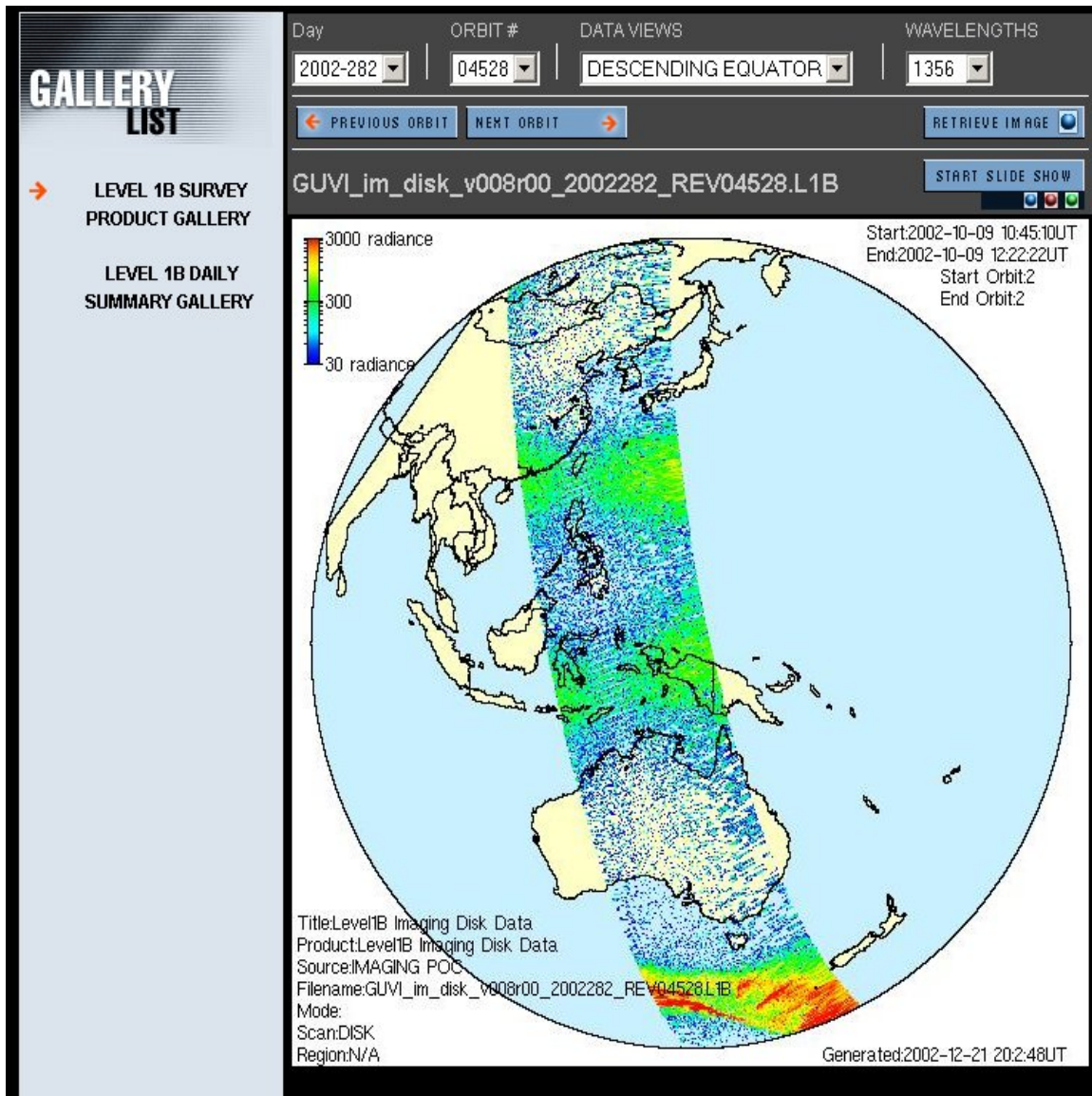


Figure 11. GUVI Web Image for Descending Day 282 of 2002. This figure illustrates web page selections and the final resulting image from the GUVI image viewing process for Day 282. The two equatorial regions of enhanced radiance indicate the location of the crests of the equatorial anomaly [JHUAPL: GUVI, 2003].

An example of an instance where two orbits were needed is Ascending Day 96. Figures 12 and 13 show Orbits 01773 and 01774, which contain the data necessary to study this day. In both ascending and descending cases, the DOY and Orbit # or Filename was important for data retrieval and therefore, recorded from the image(s).

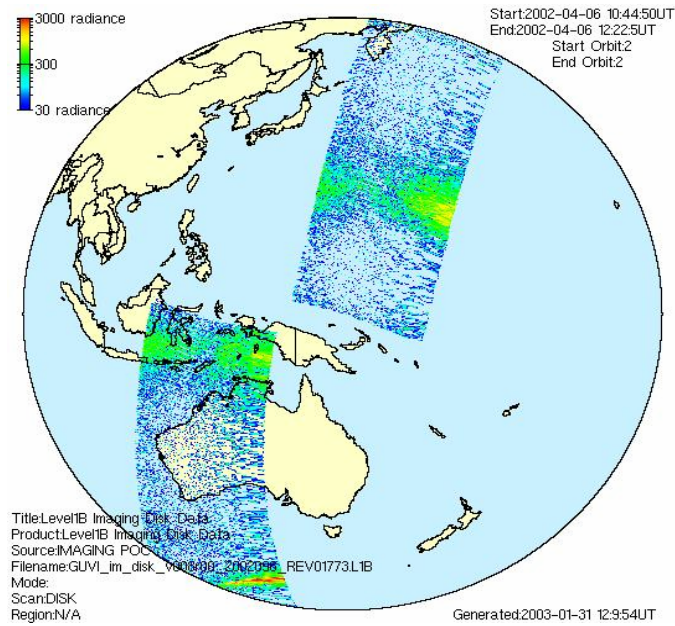


Figure 12. GUVI Image for Ascending Day 96 of 2002 - Orbit 01773. The image illustrates one of two orbits necessary to study Ascending Day 96. Only the southern anomaly peak falls within the Philippine longitude sector [JHUAPL: GUVI, 2003]

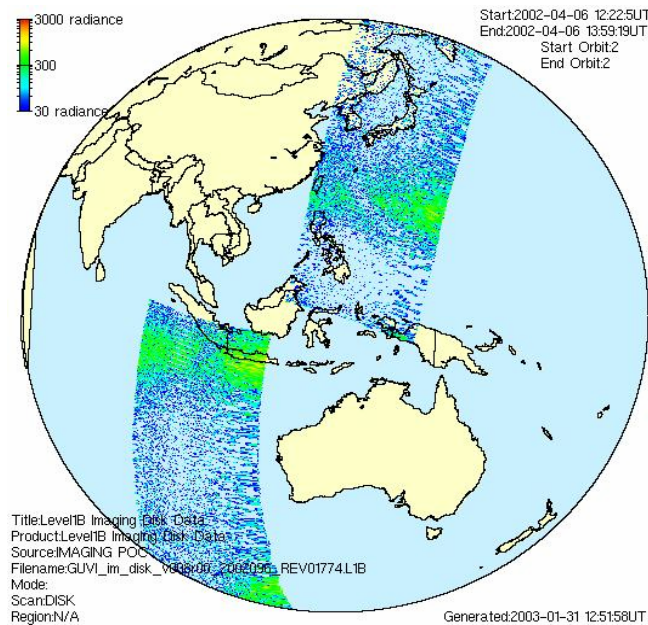


Figure 13. GUVI Image for Ascending Day 96 of 2002 - Orbit 01774. The image illustrates the other of two orbits necessary to study Ascending Day 96. Only the northern anomaly peak falls within the Philippine longitude sector [JHUAPL: GUVI, 2003]

The GUVI image viewing process can sometimes bring about the exclusion of study days. This occurred, for example, with Ascending Day 97. When viewing the images to determine the two orbits needed, it became apparent that images (and the corresponding data files) were missing for Orbits 01789 and 01790. Coincidentally, Orbits 01788 and 01789 were the orbits that contained the appropriate Philippine sector data and the day was consequently disallowed. This was the only day in my research where this occurred, but it could conceivably happen on other days that were not considered and is therefore mentioned.

GUVI Data Retrieval

In order to retrieve the appropriate GUVI data files from the following website, <http://guvi.jhuapl.edu/levels/level1b/imaging/2002/>, two types of information were needed; the day of year and the orbit number(s) (or filename(s)). The previous section discussed how to obtain this information for a specific day.

The GUVI website contains folders for each day of 2002. Within each folder is a list of several data files; one file with disk data and one with limb data for each orbit number on the specified day. Using a previous example, Descending Day 282, the two files in the folder that correspond to the orbit over the Philippine sector are:

GUVI_im_disk_v008r00_2002282_REV04528.L1B.gz

GUVI_im_limb_v008r00_2002282_REV04528.L1B.gz

The files needed in this research are those corresponding to disk data; the primary reason being that this was the data used in the Peruvian study, which proved to create a better defined relationship between latitude crest separation and average $\vec{E} \times \vec{B}$ drift velocity

[Anderson, private communication, 2003]. Therefore, for each of the days in 2002, the files of the following form, for the appropriate orbits, were downloaded.

GUVI_im_disk_v008r00_2002***_REV*****.L1B.gz

(NOTE: The first set of * implies day of year and the second set the appropriate orbit number.) In the ascending orbit cases, two files were needed for each day because there were two appropriate orbits.

IDL Code, Input, and Output

An additional reason why GUVI disk files were used was because an IDL program used to convert the data into an organized format was created to ingest these files. This program, supplied by *Anderson and Anghel* [private communication, 2003] in the form utilized in their similar Peruvian study, takes raw GUVI data (in the form of the downloaded files) and puts it into tabular form with the following column headings: No., DOY, Hr:Mn:Sc, Radiance1, Radiance2, Radiance3, Radiance4, RadianceT, Lat1, Lat2, Lat3, Lat4, LatT, Long1, Long2, Long3, Long4, and LongT.

The input data, or GUVI disk file, is a collection of radiance data saved in a $388 \times 14 \times 158$ matrix. 388 is the number of scans during one TIMED orbit, 14 is the number of pixels in latitude ($\sim 2^\circ$) for one scan, and 158 is the number of pixels in longitude ($\sim 15^\circ$) for one scan. The IDL program takes each 14×158 GUVI image (scan) and divides it into four longitude segments (Long1, Long2, Long3, and Long4). An average radiance (Radiance1, Radiance2, Radiance3, and Radiance4) is calculated for each segment in addition to an average latitude (Lat1, Lat2, Lat3, and Lat4) where the corresponding radiance occurs. The average radiance for each 14×158 image is

designated as RadianceT, and LatT and LongT are the averages in latitude and longitude, respectively [Anghel, private communication, 2003].

I made only one modification to the source code for this IDL program in order to apply it to the Philippine GUVI data. At one point, the program uses a geographic coverage region to determine whether the data is applicable to the region of study and should be included in the table. The program has latitude and longitude intervals over which it runs; if the raw GUVI data falls outside these intervals, the corresponding scans aren't included in the output file. For the Philippine sector, geographic latitudes between 40° S - 40° N and geographic longitudes from 100° E -140° E were used. Once this was changed within the source code, the IDL program could be run on each of the GUVI data files to create a data table for each studied day. This alteration is illustrated in Appendix B, which includes the source code for the Philippine version of this program.

In running the program, there was a slight difference between descending and ascending orbit data. For the descending days, only the one disk file was necessary to create an output table with all of the necessary information. However, for the ascending days, because there were two orbits and therefore two data files that each contained about half of the information, both output tables were utilized. As can be seen in the previous Figures 12 and 13, the end of the first orbit and the beginning of the second were necessary to describe the longitude sector completely. Therefore, data from the end of the first orbit's output and the beginning of the second were used to obtain the GUVI observations.

Determination of Anomaly Crest Separations

In order to determine the latitude crest separation from the GUVI data, the tabular output from the IDL program was utilized. The data needed to do this were the average radiance values (RadianceT) for each 14×158 scan, and the average latitude (LatT) corresponding to each average radiance value. As mentioned earlier, the IDL program only uses data within a specific coverage area (40° S - 40° N geog. Lat.; 100° E - 140° E geog. Long.) to produce its output, so only some of the 388 total scans were utilized.

To determine the latitude crest separation for descending orbit days, plots were made of RadianceT versus LatT from the IDL output file from that day. Figure 14 is an example based on data for Descending Day 282.

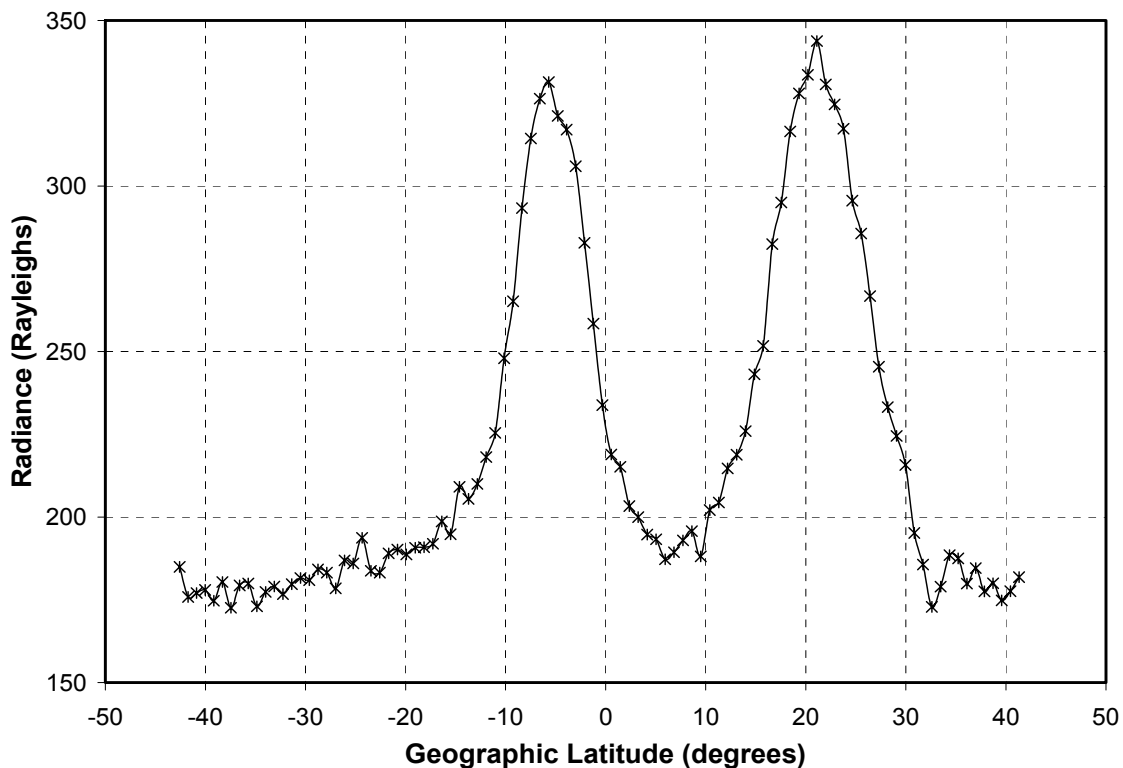


Figure 14. Plot of RadianceT (Rayleighs) versus LatT ($^\circ$) for Descending Day 282. Illustrated are two regions of enhanced radiance (equatorial anomaly peaks).

Figure 14 shows two peaks in radiance corresponding to the enhanced 1356Å airglow emissions resulting from the peaks of the equatorial anomaly. From this plot, two geographic latitudes can be extracted to determine the locations of these peaks. Furthermore, the values can be subtracted to determine the latitude crest separation of the peaks on this day. In the above case, Descending Day 282, the peak in the southern hemisphere is located at a geographic latitude of -5.68° , the peak in the northern hemisphere is located at 21.11° , and the resulting crest separation is 26.79° .

When using this same technique for ascending orbit days, data from two orbits was utilized to produce a plot as in Figure 15, which illustrates this.

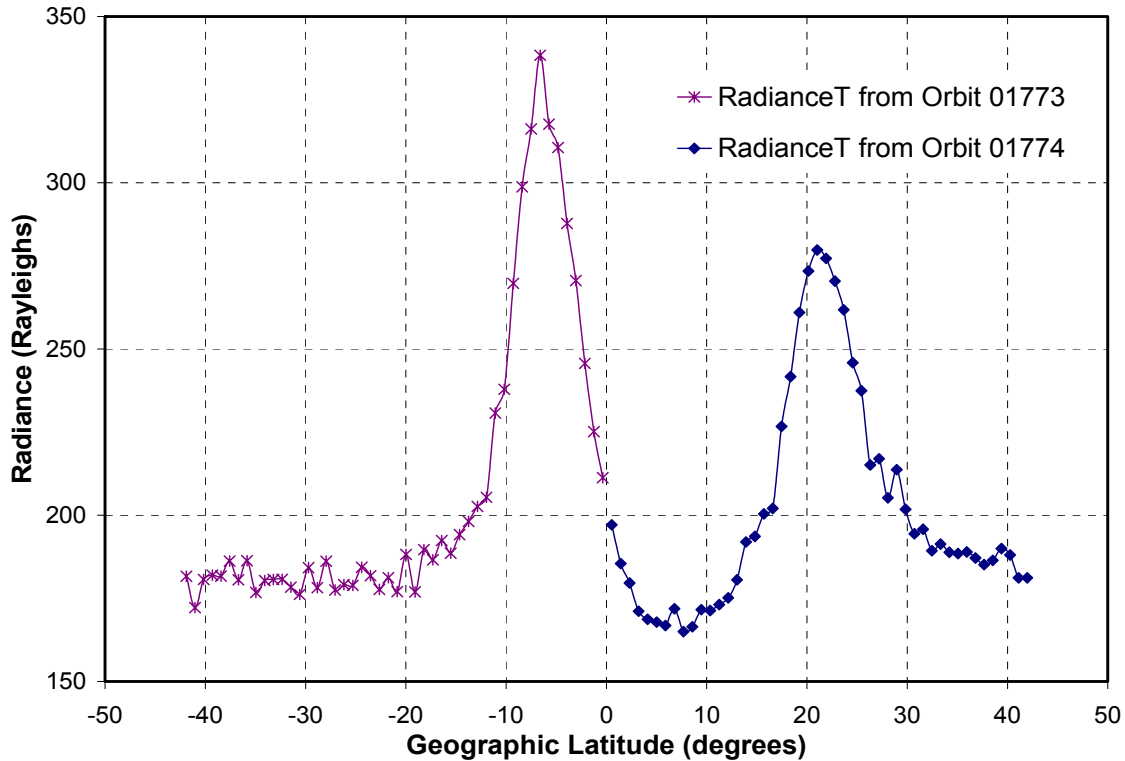


Figure 15. Plot of RadianceT (Rayleighs) versus LatT ($^\circ$) for Ascending Day 96. The plot illustrates two regions of enhanced radiance (equatorial anomaly peaks). Orbit 01773 shows data for the anomaly peak in the southern hemisphere and Orbit 01774 shows data for the northern peak.

In this ascending case, Day 96, the southern hemisphere peak is located at a geographic latitude of -6.61° , the northern peak is located at 21.02° , and the resulting crest separation is 27.63° .

In some cases, however, two radiance peaks did not exist and a resulting crest separation could not be determined. These days were excluded from further study. Two examples of these instances are illustrated in the following Figures 16 and 17.

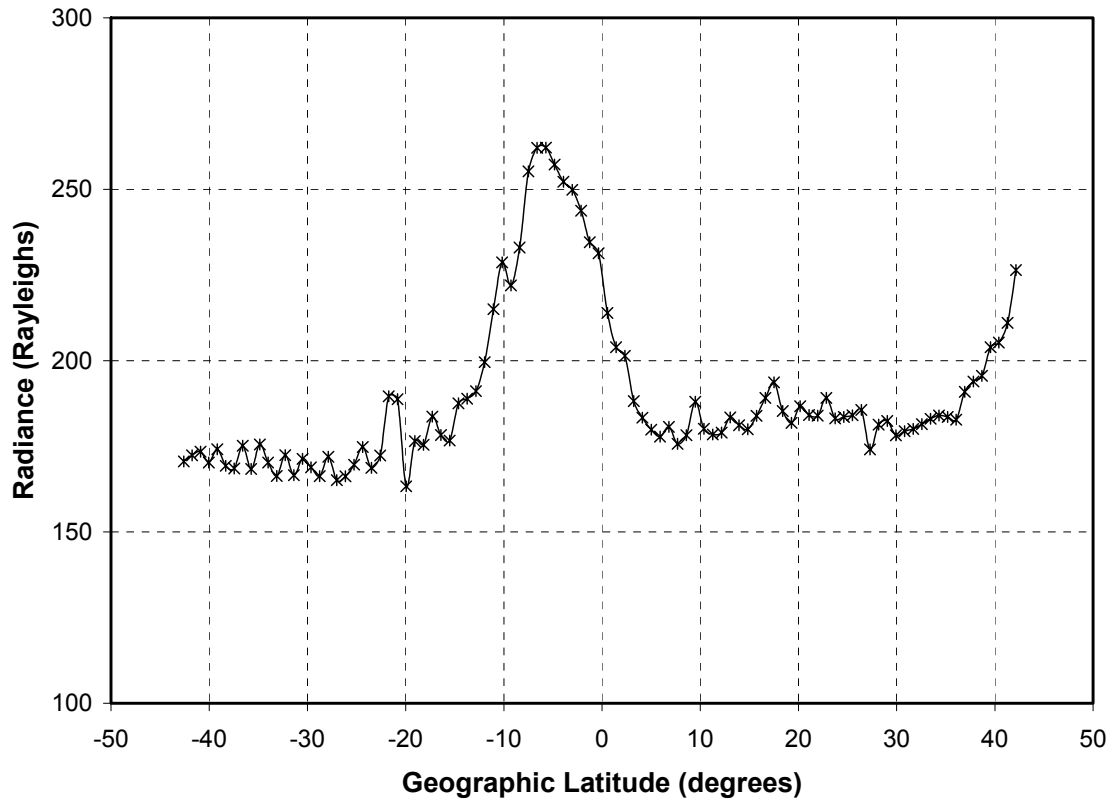


Figure 16. Plot of RadianceT (Rayleighs) versus LatT ($^\circ$) for Descending Day 156. The plot illustrates only one region of enhanced radiance.

In total, 10 days (44, 156, 157, 159, 160, 161, 162, 164, 277, and 291) were excluded because two distinct peaks could not be distinguished in order to determine an anomaly crest separation.

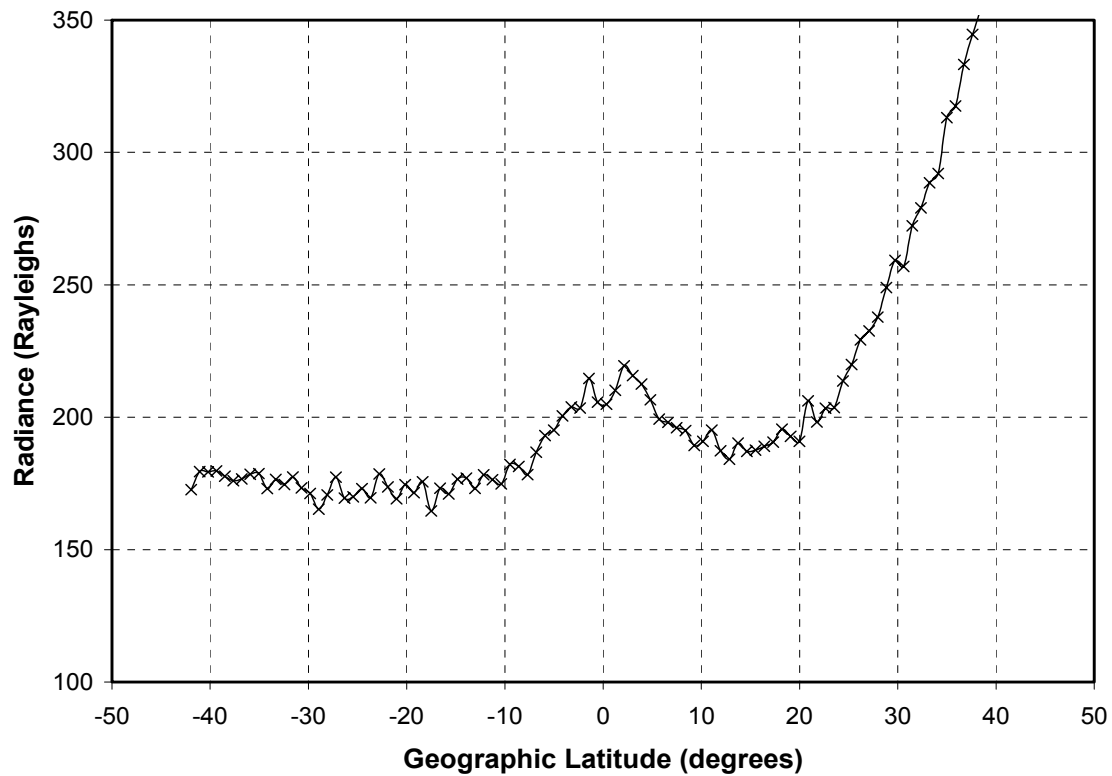


Figure 17. Plot of RadianceT (Rayleighs) versus LatT (°) for Descending Day 162. The plot illustrates only one region of enhanced radiance.

At this point, all days that were going to be excluded from the study had been determined. Therefore, I will again list the sets of days with the excluded days omitted:

Descending (43 Days):

Initial Group (15 Days): 35, 38, 39, 40, 41, 42, 43, 45, 281, 282, 285, 286, 287, 289, 290

Additional Group (28 Days): 26, 27, 28, 29, 30, 31, 32, 33, 34, 36, 37, 151, 152, 153, 155, 158, 163, 271, 272, 273, 276, 278, 279, 280, 283, 284, 288, 292

Ascending (13 Days): 91, 94, 95, 96, 98, 99, 100, 101, 102, 103, 106, 107, 110

Tables 1 and 2 provide the orbit number(s) for all GUVI data used. Also included are the locations for the northern and southern equatorial anomaly peaks for each of the remaining days and the latitude crest separation between the peaks.

Table 1. Anomaly Peak Locations and Crest Separation for All Ascending Days

DOY	Orbits Used	Southern Peak Latitude (°)	Northern Peak Latitude (°)	Latitude Crest Separation (°)
91	01700-01701	-6.98	21.54	28.52
94	01744-01745	-7.23	22.18	29.41
95	01759-01760	-6.91	24.26	31.17
96	01773-01774	-6.61	21.02	27.63
98	01803-01804	-5.19	23.31	28.50
99	01817-01818	-9.31	25.42	34.73
100	01832-01833	-5.34	22.28	27.62
101	01847-01848	-5.82	22.70	28.52
102	01861-01862	-6.30	23.10	29.40
103	01876-01877	-5.85	21.78	27.63
106	01920-01921	-7.88	23.30	31.18
107	01935-01936	-8.17	24.78	32.95
110	01979-01980	-5.52	21.22	26.74

Table 2. Anomaly Peak Locations and Crest Separation for All Descending Days

DOY	Orbits Used	Southern Peak Latitude (°)	Northern Peak Latitude (°)	Latitude Crest Separation (°)
26	00738	-5.39	21.37	26.76
27	00753	-3.83	22.02	25.85
28	00768	-3.21	19.09	22.30
29	00782	-6.23	24.96	31.19
30	00797	-7.45	20.20	27.65
31	00812	-10.48	21.62	32.10
32	00826	-3.82	19.37	23.19
33	00841	-6.02	22.51	28.53
34	00856	-6.41	23.02	29.43
35	00870	-7.85	21.58	29.43
36	00885	-7.45	22.87	30.32
37	00900	-5.28	22.36	27.64
38	00914	-5.90	21.74	27.64
39	00929	-8.25	22.06	30.31
40	00944	-8.90	24.97	33.87
41	00958	-9.58	25.17	34.75
42	00973	-7.54	22.17	29.71
43	00988	-5.52	22.12	27.64
45	01017	-4.29	23.34	27.63
151	02589	-3.81	20.30	24.11
152	02603	-5.91	22.65	28.56
153	02618	-6.27	22.29	28.56
155	02648	-5.41	24.03	29.44
158	02692	-5.99	21.68	27.67
163	02765	-6.43	23.91	30.34
271	04367	-5.10	19.91	25.01
272	04381	-3.01	20.21	23.22
273	04396	-3.77	22.12	25.89
276	04440	-4.55	19.56	24.11
278	04469	-4.24	19.87	24.11
279	04484	-3.24	16.41	19.65
280	04499	-6.78	21.79	28.57
281	04513	-3.00	19.33	22.33
282	04528	-5.68	21.11	26.79
283	04543	-8.37	23.76	32.13
284	04558	-9.29	23.74	33.03
285	04572	-5.57	21.22	26.79
286	04587	-6.52	22.94	29.46
287	04602	-6.65	21.92	28.57
288	04616	-3.88	19.35	23.23
289	04631	-5.65	22.91	28.56
290	04646	-4.89	21.90	26.79
292	04675	-5.90	22.67	28.57

Determining the $\vec{E} \times \vec{B}$ Drift Velocity from Anomaly Crest Separations

At this point, the expression from the Peruvian study could be applied to the latitude crest separations extracted from GUVI. This expression is Equation (6) from the previous chapter.

The expression was applied to the crest separations to produce an inferred, average vertical drift velocity for each of the studied days. Tables 3 and 4 provide the crest separation and corresponding $\vec{E} \times \vec{B}$ drift velocity for each day:

Table 3. Latitude Crest Separation & Inferred $\vec{E} \times \vec{B}$ Drift Velocity (Ascending Days)

DOY	Latitude Crest Separation (°)	Inferred $\vec{E} \times \vec{B}$ Drift Velocity (m/s)
91	28.52	10.58
94	29.41	11.43
95	31.17	13.10
96	27.63	9.73
98	28.50	10.56
99	34.73	16.50
100	27.62	9.72
101	28.52	10.58
102	29.40	11.42
103	27.63	9.73
106	31.18	13.11
107	32.95	14.80
110	26.74	8.89

Table 4. Latitude Crest Separation & Inferred $\vec{E} \times \vec{B}$ Drift Velocity (Descending Days)

DOY	Latitude Crest Separation (°)	Inferred $\vec{E} \times \vec{B}$ Drift Velocity (m/s)
26	26.76	8.90
27	25.85	8.04
28	22.30	4.66
29	31.19	13.12
30	27.65	9.75
31	32.10	13.99
32	23.19	5.50
33	28.53	10.59
34	29.43	11.45
35	29.43	11.45
36	30.32	12.30
37	27.64	9.74
38	27.64	9.74
39	30.31	12.29
40	33.87	15.68
41	34.75	16.51
42	29.71	11.71
43	27.64	9.74
45	27.63	9.73
151	24.11	6.38
152	28.56	10.62
153	28.56	10.62
155	29.44	11.46
158	27.67	9.77
163	30.34	12.31
271	25.01	7.24
272	23.22	5.53
273	25.89	8.08
276	24.11	6.38
278	24.11	6.38
279	19.65	2.13
280	28.57	10.63
281	22.33	4.69
282	26.79	8.93
283	32.13	14.02
284	33.03	14.88
285	26.79	8.93
286	29.46	11.48
287	28.57	10.63
288	23.23	5.54
289	28.56	10.62
290	26.79	8.93
292	28.57	10.63

Magnetometer Data Retrieval and Averaging

Once the inferred, average, vertical $\vec{E} \times \vec{B}$ drift velocity was determined, the average ΔH was determined for each day. The magnetometer data was obtained via FTP transfer [Anderson and Anghel, private communication, 2003]. The files with data for the initial set of descending days and all of the ascending days were simple two-column data files providing an average ΔH and time in LT at five minute intervals from 0800 LT to 1700 LT. When the magnetometer data for the additional set of descending days were obtained, these data were still given at five minute intervals, but data were provided from 0-2400 UT. Data from 0000-0900 UT corresponds to 0800-1700 LT, so these data were extracted from these files. An average ΔH for the entire nine hour period was computed by averaging the five minute average values. This nine hour average was representative of the daily average ΔH component resulting from the daytime geomagnetic variation attributed to the Sq current system and resulting equatorial electrojet. Tables 5 and 6 provide a summary of the results to this point, including the daily average ΔH values; all was used later to construct ΔH versus $\vec{E} \times \vec{B}$ regression relationships.

Table 5. Crest Separation, Inferred Drift Velocity, & Average ΔH (Ascending Days)

DOY	Latitude Crest Separation (°)	Inferred $\vec{E} \times \vec{B}$ (m/s)	Average ΔH (nT)
91	28.52	10.58	34.078554
94	29.41	11.43	44.018885
95	31.17	13.10	39.002202
96	27.63	9.73	28.625890
98	28.50	10.56	35.493788
99	34.73	16.50	70.750587
100	27.62	9.72	46.332080
101	28.52	10.58	46.643753
102	29.40	11.42	60.801141
103	27.63	9.73	45.657425
106	31.18	13.11	61.083832
107	32.95	14.80	67.203010
110	26.74	8.89	30.688371

Table 6. Crest Separation, Inferred Drift Velocity, & Average ΔH (Descending Days)

DOY	Latitude Crest Separation (°)	Inferred $\vec{E} \times \vec{B}$ (m/s)	Average ΔH (nT)
26	26.76	8.90	18.988953
27	25.85	8.04	53.592001
28	22.30	4.66	25.340265
29	31.19	13.12	60.146519
30	27.65	9.75	47.202635
31	32.10	13.99	49.964828
32	23.19	5.50	41.651973
33	28.53	10.59	64.634190
34	29.43	11.45	45.269006
35	29.43	11.45	87.145321
36	30.32	12.30	63.792588
37	27.64	9.74	43.226089
38	27.64	9.74	46.067771
39	30.31	12.29	40.569524
40	33.87	15.68	60.207372
41	34.75	16.51	63.441293
42	29.71	11.71	55.396482
43	27.64	9.74	46.765027
45	27.63	9.73	68.850785
151	24.11	6.38	37.796435
152	28.56	10.62	56.849891
153	28.56	10.62	43.028199
155	29.44	11.46	35.293184
158	27.67	9.77	43.962875
163	30.34	12.31	37.200039
271	25.01	7.24	33.534012
272	23.22	5.53	50.866048
273	25.89	8.08	39.628070
276	24.11	6.38	53.729508
278	24.11	6.38	46.666770
279	19.65	2.13	27.561851
280	28.57	10.63	64.193663
281	22.33	4.69	49.585267
282	26.79	8.93	69.979874
283	32.13	14.02	45.841465
284	33.03	14.88	54.367804
285	26.79	8.93	40.709118
286	29.46	11.48	54.063198
287	28.57	10.63	42.352462
288	23.23	5.54	26.602812
289	28.56	10.62	42.047456
290	26.79	8.93	43.811611
292	28.57	10.63	46.988986

The two previous tables include a summary of the primary results needed to formulate the relation that is the goal of this research. The remainder of this chapter will include a description of how this data was manipulated in order to produce the best final expression for a Philippine sector, average ΔH versus inferred $\vec{E} \times \vec{B}$ regression relation.

Regression Development

Now that the average ΔH values and inferred $\vec{E} \times \vec{B}$ drift velocities had been computed for each day, the next step was to begin plotting the values to create linear regression relationships. The easiest regression set to plot initially was the entire set of days. Therefore, all 56 days were plotted together in Figure 18.

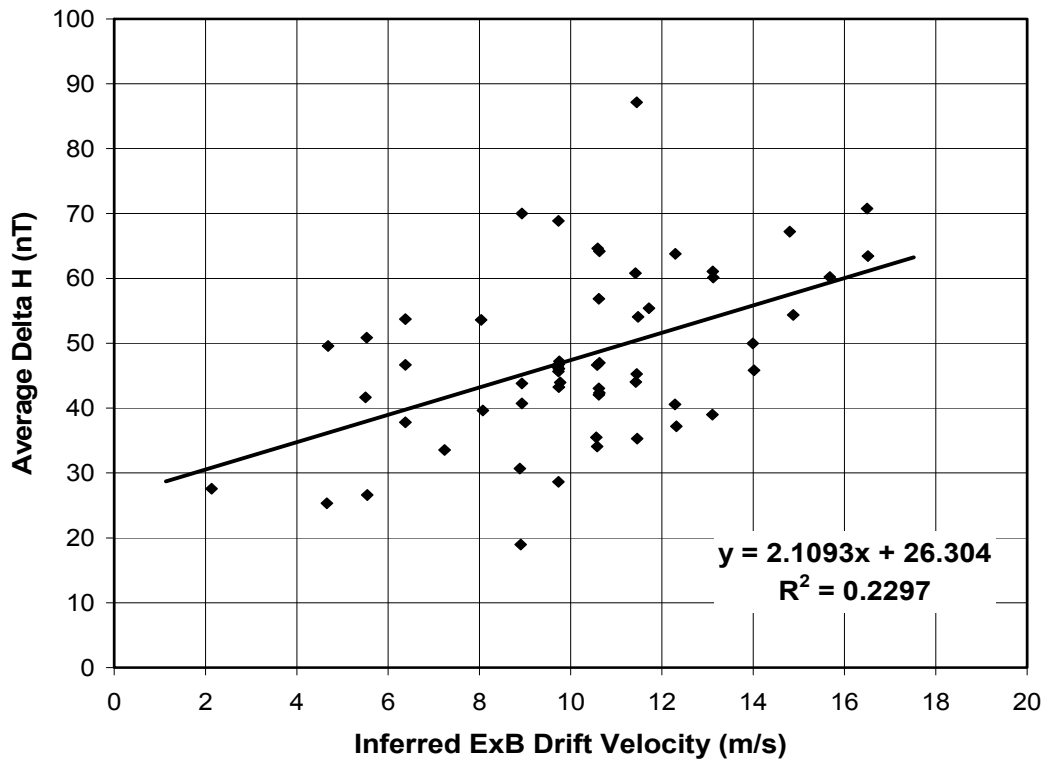


Figure 18. Regression Relation for Average ΔH (nT) versus Inferred $\vec{E} \times \vec{B}$ Drift Velocity (m/s) for All 56 Study Days, Ascending and Descending.

As can be seen by Figure 18, Excel was used to calculate R^2 (a statistical measure of how well the regression approximates the data) for this regression. The resulting value is only 0.2297, where an R^2 of 1.0 is indicative of a perfect fit. Because this number is far from 1, our confidence in the quality of this fit is small.

After seeing the R^2 for the data set as a whole, it was decided upon to maintain the ascending/descending divisions in data so that an attempt could be made to derive a better regression. Therefore, two regressions were determined; one for the ascending days and another for the descending days. These plots can be found in Figures 19 and 20.

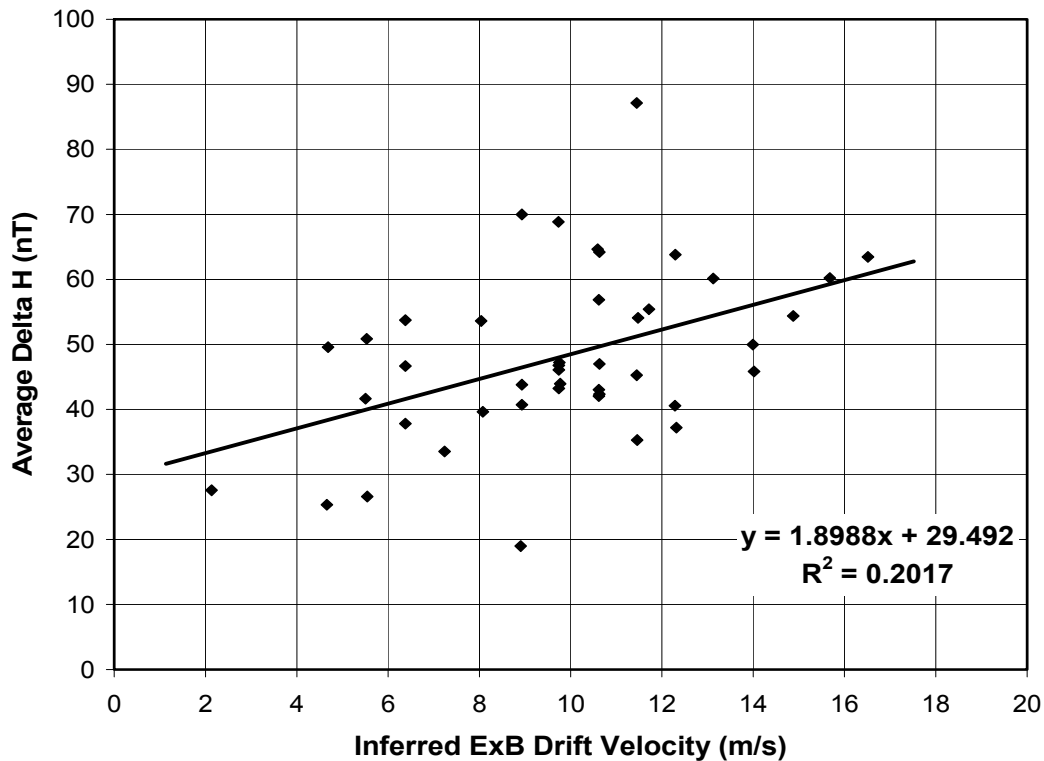


Figure 19. Regression Relation for Average ΔH (nT) versus Inferred $\vec{E} \times \vec{B}$ Drift Velocity (m/s) for All 43 Descending Days.

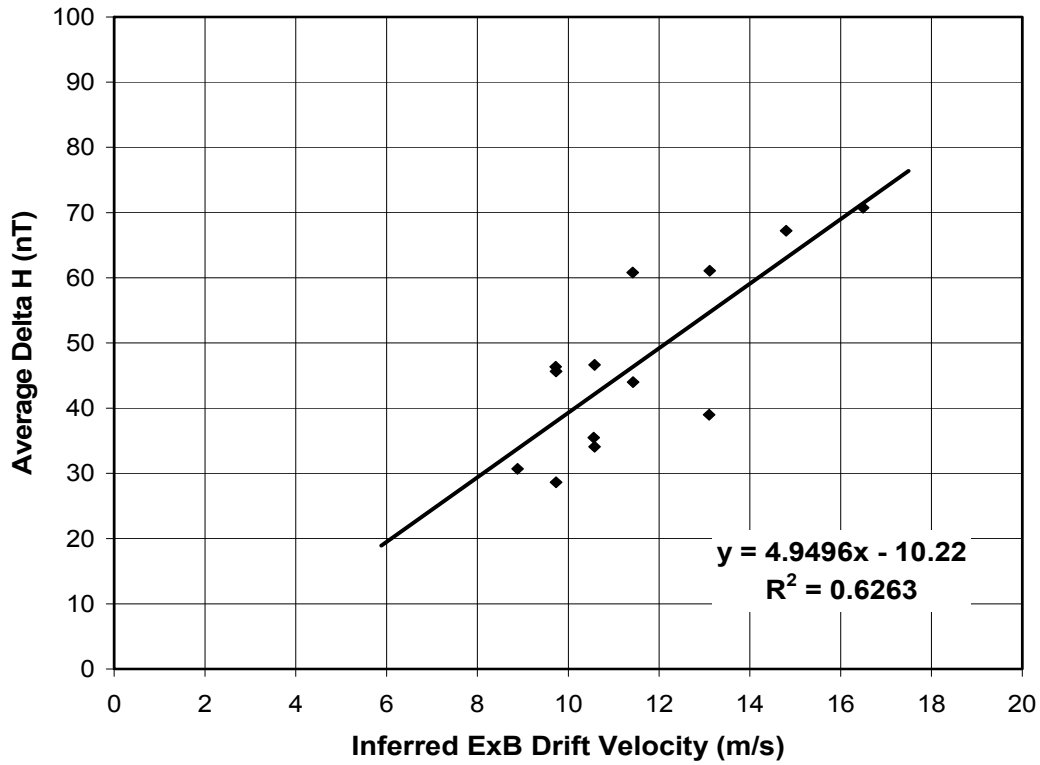


Figure 20. Regression Relation for Average ΔH (nT) versus Inferred $\vec{E} \times \vec{B}$ Drift Velocity (m/s) for All 13 Ascending Days.

As these figures show, the set of descending days produces a regression with too small of an R^2 value; only 0.2017. However, for the ascending days, the R^2 is 0.6263. The fit for the ascending set of days is a vast improvement on both the descending only and combined data sets. The reason(s) for the large differences in the ascending versus descending correlations is presently unknown.

Statistics

Some basic statistics were applied at this point in order to eliminate outlying points and possibly improve the R^2 values for these regression relations. The first data

set considered will be the combined ascending and descending set (i.e. all 56 days). The following process was used to eliminate points:

1. Using the regression relation that resulted from plotting average ΔH versus inferred $\vec{E} \times \vec{B}$ drift for all 56 days, I substituted each calculated $\vec{E} \times \vec{B}$ drift into the equation and solved for what ΔH “should be” for that drift based on the regression.
2. I subtracted this calculated ΔH from the measured ΔH that was initially used to create the regression. This provided me with a list of differences in ΔH ; the mean of the set of differences was nearly zero.
3. I then removed all days that had a ΔH difference outside of two standard deviations from the mean of this ΔH difference set.
4. The remaining days were plotted, as in Figure 21, to form a new regression relation.

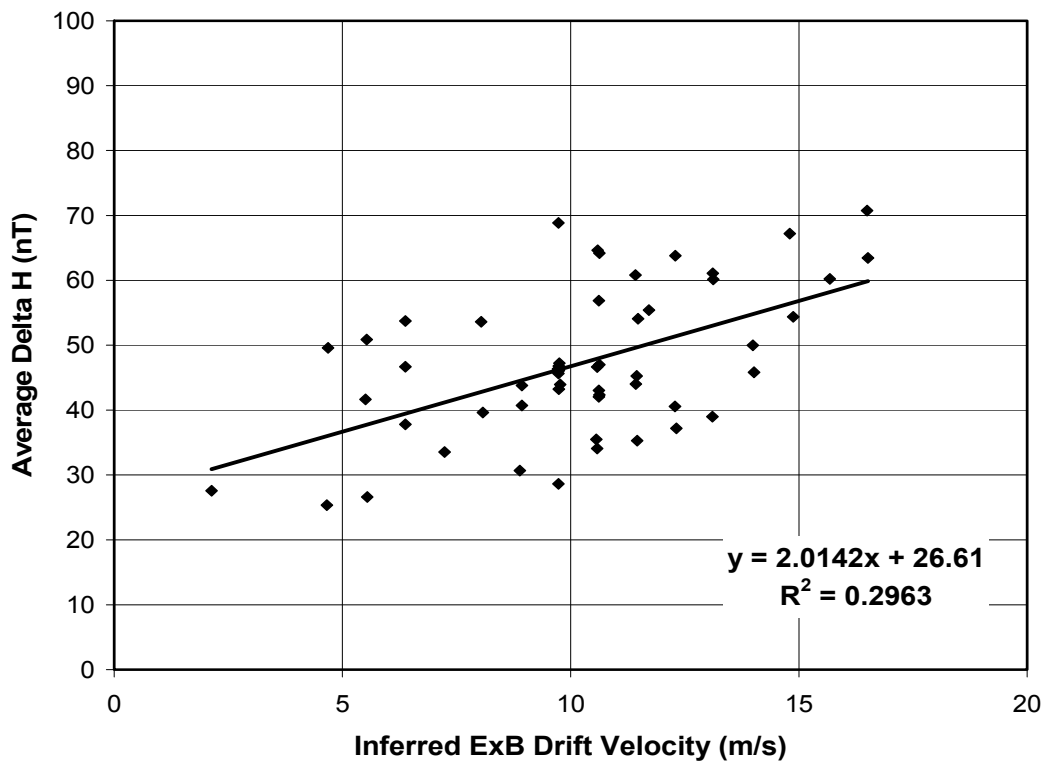


Figure 21. New Regression for All 56 Study Days (Ascending & Descending) with Points Outside Two Standard Deviations Removed.

As can be seen by the previous figure, both the regression relation and R^2 value changed. From the initial relation in Figure 18 to the corrected relation in Figure 21, we see that the regression changed from:

$$\begin{aligned} \Delta H &= 2.1093 (\bar{E} \times \bar{B}) + 26.304 \\ &\text{to} \\ \Delta H &= 2.0142 (\bar{E} \times \bar{B}) + 26.61 \end{aligned}$$

Also, the R^2 increased from 0.2297 to 0.2963. Although this was not a drastic change, the process did seem to improve both the regression and R^2 . Therefore, this process was also performed on the ascending and descending sets separately in order to maintain any inherent differences between the two. Also, the ascending only regression relation was so much better than that of the descending only or combined sets that I wanted to see how much I could improve on this relationship.

After completing this process on the descending only set of days, only two of the 43 days (DOY 26 and 35) could be removed. The regression relation changed from:

$$\begin{aligned} \Delta H &= 1.8988 (\bar{E} \times \bar{B}) + 29.492 \\ &\text{to} \\ \Delta H &= 1.691 (\bar{E} \times \bar{B}) + 31.319 \end{aligned}$$

The R^2 , however, only increased from 0.2017 to 0.2354. Even more unfortunate was that when the process was completed for the ascending set of days, none of the days could be eliminated and therefore, the regression and R^2 were unchanged. If points greater than only 1 deviation were removed, the regression did improve, but because the total ascending data set contained only 13 days, it was not plausible to do so. For the descending data set, about 1/3 of the 43 days would have been removed if points outside

only one standard deviation had been eliminated; again showing that a limit of two standard deviations was more reasonable.

Attempted Validation by Partitioning of Descending Data

Recall that the descending data is divided into two subsets: an initial set and an additional set. An attempt was made to validate a descending data regression relation by using the initial set of descending days to establish a ΔH versus $\vec{E} \times \vec{B}$ regression relation, then verifying against the additional set of descending days. This technique has already been used by *Anderson and Anghel* [private communication, 2003], and is accomplished as follows. Table 7 summarizes this effort.

1. Again, the initial set of descending days was chosen as the regression set and the additional set was the verification set.
2. The previously discussed process was used to form a regression relation using only the initial set of days, with points greater than two standard deviations removed. The resulting relation is: $\Delta H = 0.9664 (\vec{E} \times \vec{B}) + 41.375$
3. The $\vec{E} \times \vec{B}$ drift velocities for each of the additional (verification) descending days were substituted into the regression to determine a “regression computed” ΔH value.
4. A scatter plot was created with the “regression computed” ΔH values on the x-axis and the corresponding average daily ΔH values computed from the magnetometer data on the y-axis. If the regression line created using the initial (regression) set of days is good, the slope of the scatter plot should be close to 1.

Table 7. Additional (Verification) Descending Day Data Used to Validate the Initial Descending Day Regression Relation

DOY	Inferred $\vec{E} \times \vec{B}$ (m/s)	Average Daily ΔH from Magnetometer (nT)	Regression Computed ΔH (nT)
26	8.90	18.988953	49.98
27	8.04	53.592001	49.14
28	4.66	25.340265	45.88
29	13.12	60.146519	54.05
30	9.75	47.202635	50.80
31	13.99	49.964828	54.89
32	5.50	41.651973	46.69
33	10.59	64.634190	51.61
34	11.45	45.269006	52.44
36	12.30	63.792588	53.26
37	9.74	43.226089	50.79
151	6.38	37.796435	47.54
152	10.62	56.849891	51.64
153	10.62	43.028199	51.64
155	11.46	35.293184	52.45
158	9.77	43.962875	50.82
163	12.31	37.200039	53.27
271	7.24	33.534012	48.37
272	5.53	50.866048	46.72
273	8.08	39.628070	49.18
276	6.38	53.729508	47.54
278	6.38	46.666770	47.54
279	2.13	27.561851	43.43
280	10.63	64.193663	51.65
283	14.02	45.841465	54.92
284	14.88	54.367804	55.76
288	5.54	26.602812	46.73
292	10.63	46.988986	51.65

Figure 22 is a plot of the ΔH values with the equation of the trendline included in order to determine the slope of the line.

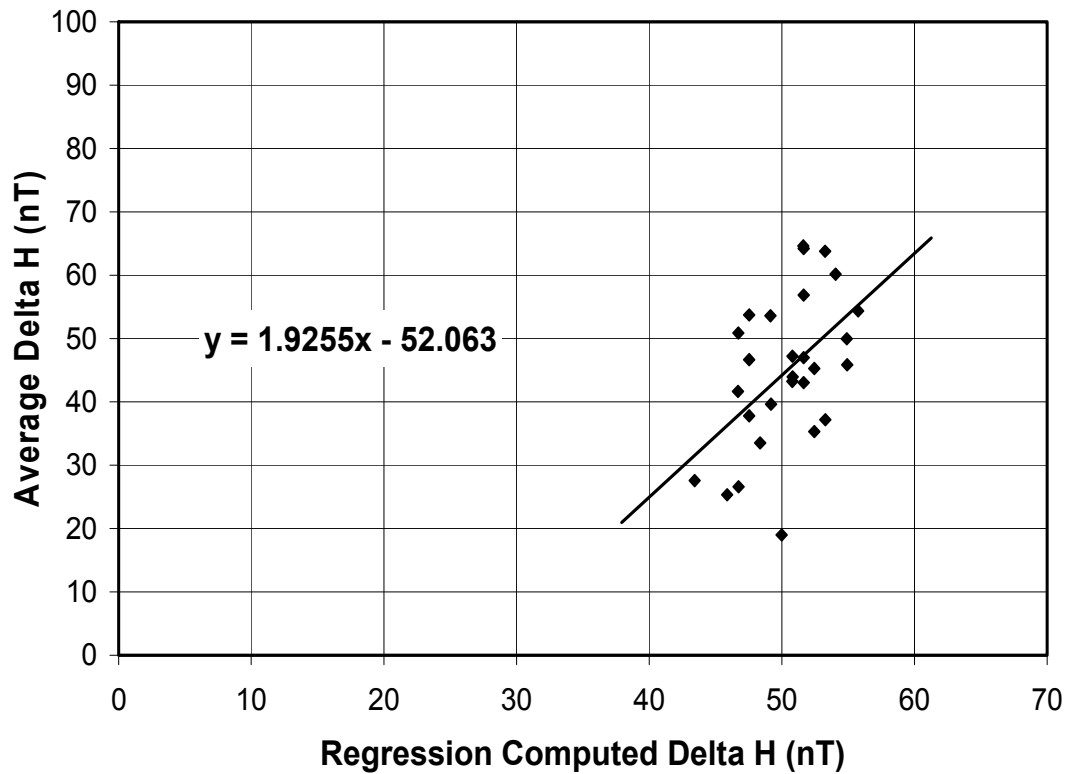


Figure 22. Average Daily ΔH from Magnetometer Data versus Regression Computed ΔH . The Initial Descending Days are the regression set and the Additional Descending Days are the verification set.

This process was repeated, this time using the additional set of descending days as the regression set and the initial set of days as the verification set. The regression relation resulting from the additional (regression) set of days with points greater than two standard deviations removed is: $\Delta H = 1.8229 (\bar{E} \times \bar{B}) + 28.89$. The drift velocity values for the initial (verification) descending days were used to calculate the “regression computed” ΔH values. The following table, Table 8, illustrates this and Figure 23 shows a plot of the ΔH values.

Table 8. Initial (Verification) Descending Day Data Used to Validate the Additional Descending Day Regression Relation

DOY	Inferred $\vec{E} \times \vec{B}$ (m/s)	Average Daily ΔH from Magnetometer (nT)	Regression Computed ΔH (nT)
35	11.45	87.145321	49.76
38	9.74	46.067771	46.65
39	12.29	40.569524	51.29
40	15.68	60.207372	57.47
41	16.51	63.441293	58.99
42	11.71	55.396482	50.24
43	9.74	46.765027	46.65
45	9.73	68.850785	46.63
281	4.69	49.585267	37.44
282	8.93	69.979874	45.17
285	8.93	40.709118	45.17
286	11.48	54.063198	49.82
287	10.63	42.352462	48.27
289	10.62	42.047456	48.25
290	8.93	43.811611	45.17

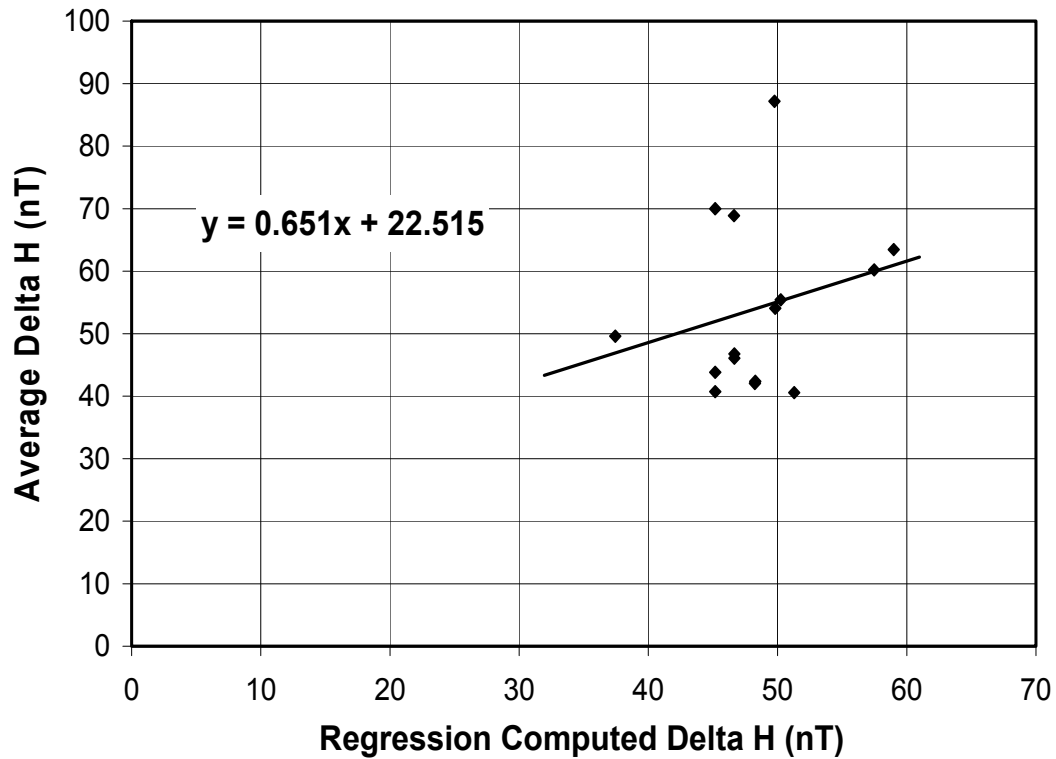


Figure 23. Average Daily ΔH from Magnetometer Data versus Regression Computed ΔH with Regression and Verification Sets Switched. The Initial Descending Days are now the regression set and the Additional Descending Days are the verification set.

As can be seen by Figures 22 and 23, neither slope is very close to 1, implying that neither regression is acceptably accurate.

Clearly, maintaining a data division based only on the criteria of ascending or descending orbits was not providing very good results, and so a new approach was taken.

Division by Month and Season

At this point in the research, the best correlated regression relation resulted from using only the ascending days. When looking more specifically at these ascending days, it can be seen that they are grouped so closely together that they each occurred during the month of April. Now, as might be expected, the $F_{10.7}$ index (the solar radio flux at a wavelength of 10.7 cm at Earth's orbit) among the ascending days is rather comparable. The $F_{10.7}$ index is indicative of the level of solar activity, which of course is a factor in the amount of solar UV available to ionize the Earth's upper atmosphere. As a result of the temporal variation in this index, I regrouped the descending days by month and also by season. This made it possible to keep $F_{10.7}$ (and solar activity) consistent within each descending sub-group, which included days from the summer, winter, and fall. Table 9 provides the $F_{10.7}$ index for each month in 2002.

The monthly sub-groupings were as follows:

January: 26, 27, 28, 29, 30, 31

February: 32, 33, 34, 35, 36, 37, 38, 39, 40, 41, 42, 43, 45

April (ascending): 91, 94, 95, 96, 98, 99, 100, 101, 102, 103, 106, 107, 110

May: 151

June: 152, 153, 155, 158, 163

September: 271, 272, 273

October: 276, 278, 279, 280, 281, 282, 283, 284, 285, 286, 287, 288, 289, 290, 292

There were no days from the months of March, July, August, November, and December.

Table 9. Preliminary, Observed Monthly Mean Values of the Solar $F_{10.7}$ Index for 2002

Month	Radio Flux	
	Observed 10.7 cm	Smoothed 10.7 cm
01	227.3	194.6
02	205.0	197.2
03	180.3	195.7
04	189.8	191.5
05	178.4	188.0
06	148.7	183.0
07	173.5	176.3
08	183.9	169.5
09	175.8	164.1
10	167.0	159.4
11	168.7	154.8
12	158.6	150.9

[NOAA Space Environment Center, 2004]

As can be seen by the monthly sub-groups, there existed only one day in May, three days in September, and so on. The groupings were very small and were therefore regrouped by season as seen below:

Winter (January & February): 26, 27, 28, 29, 30, 31, 32, 33, 34, 35, 36, 37, 38, 39, 40, 41, 42, 43, 45

Spring (April): 91, 94, 95, 96, 98, 99, 100, 101, 102, 103, 106, 107, 110

Summer (May & June): 151, 152, 153, 155, 158, 163

Fall (September & October): 271, 272, 273, 276, 278, 279, 280, 281, 282, 283, 284, 285, 286, 287, 288, 289, 290, 292

Regrouping the days in this manner allowed for slightly larger groups, and hopefully better statistics.

For completeness, average ΔH versus inferred $\vec{E} \times \vec{B}$ regressions were still plotted by month. This was done because in previous studies in Peru, regression relationships were computed by month. Doing so in this study gave some grounds for comparison. The following plot, Figure 24, illustrates the regression relation for each monthly grouping of days. Keeping in mind that May had only one day, Day 151 (31 May 2002),

it made sense to group this day with the June set, especially because of where it falls chronologically relative to the other days in June (152, 153, 155, 158, 163).

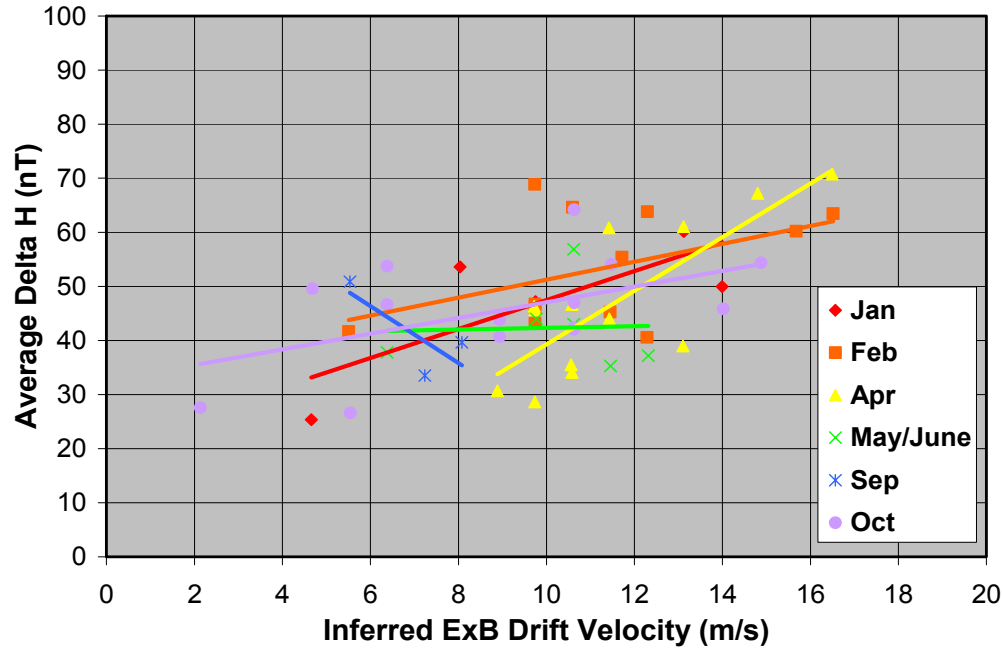


Figure 24. Average ΔH versus Inferred $\vec{E} \times \vec{B}$ Drift Velocity by Month with Points Outside Two Standard Deviations Removed.

Table 10 provides the slope and y-intercept for each of the regression relations plotted in Figure 24. The R^2 values for these 6 monthly groupings are also included, in addition to the slope of the regression when the y-intercept was forced to zero; in other words, forcing a 0-offset (to be discussed later).

Table 10: Regression Slopes, y-Intercepts, and Correlation Coefficients (R^2) by Monthly Sub-grouping

Month	Slope	y-Intercept	Correlation Coefficient	0-Offset Slope
January	2.6807	20.677	0.6017	4.5461
February	1.6571	34.681	0.2122	4.5635
April	4.9496	-10.22	0.6263	4.0943
May/June	0.1559	40.766	0.0017	4.0237
September	-5.2623	77.911	0.6015	5.6953
October	1.4529	32.547	0.2693	4.6503

The January and September correlation coefficients can seem a bit misleading due to the small data groups (6 and 3 days respectively). April (the ascending only data), as before, remains the most realistic.

An adjustment to the regression relation was made by *Anderson and Anghel* [private communication, 2003]. Assuming that ΔH of zero corresponds to a negligible equatorial electrojet, and thus a negligible vertical $\vec{E} \times \vec{B}$ drift, *Anderson* “forced” his monthly regression relations to have a y-intercept of zero (0-offset), then re-evaluated the slopes (See Table 10 for these values for the monthly sub-groups). We therefore performed the same manipulation to our Philippine results and compared against the Peruvian results.

The following figure, Figure 25 is the same as Figure 24, except with 0-offset. Again, the slopes of these regressions can be found in Table 10.

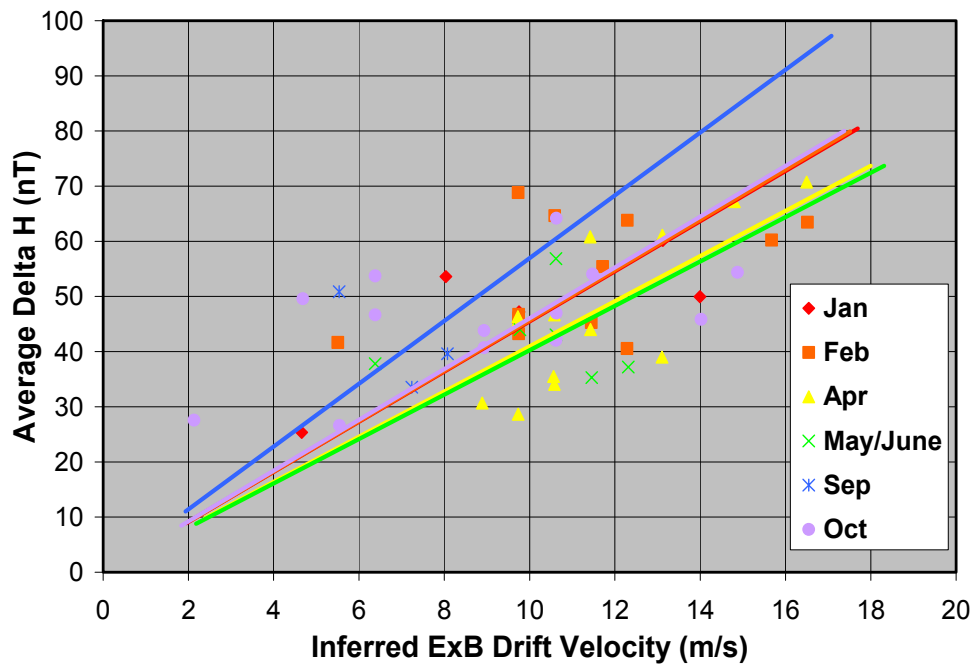


Figure 25. Average ΔH versus Inferred $\vec{E} \times \vec{B}$ Drift Velocity by Month with Points Outside Two Standard Deviations Removed and 0-Offset.

At this point, the seasonal sub-groupings were used and plotted in the same manner as the monthly sub-groupings, as can be seen by Figure 26.

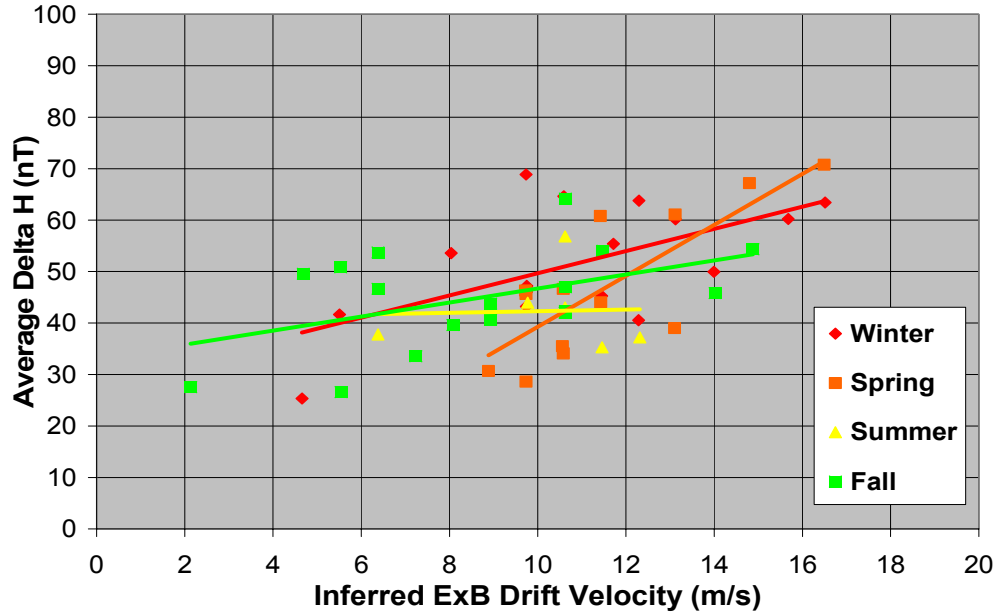


Figure 26. Average ΔH versus Inferred $\vec{E} \times \vec{B}$ Drift Velocity by Season with Points Outside Two Standard Deviations Removed.

Table 11, similar to Table 10, provides the slope and y-intercept for each of the seasonal regression relations plotted in Figure 26. The R^2 values for these 4 seasonal groupings and the slope of the regression when forced to 0-offset are also included.

Table 11: Regression Slopes, y-Intercepts, and Correlation Coefficients (R^2) by Seasonal Sub-grouping

Season	Slope	y-Intercept	Correlation Coefficient	0-Offset Slope
Winter	2.1528	28.165	0.3598	4.5591
Spring	4.9496	-10.22	0.6263	4.0943
Summer	0.1559	40.766	0.0017	4.0237
Fall	1.3648	33.078	0.2231	4.7169

Figure 27 is the same as Figure 26, except it illustrates the 0-offset version of the seasonal regressions. Table 11 provides the 0-offset slopes from Figure 27.

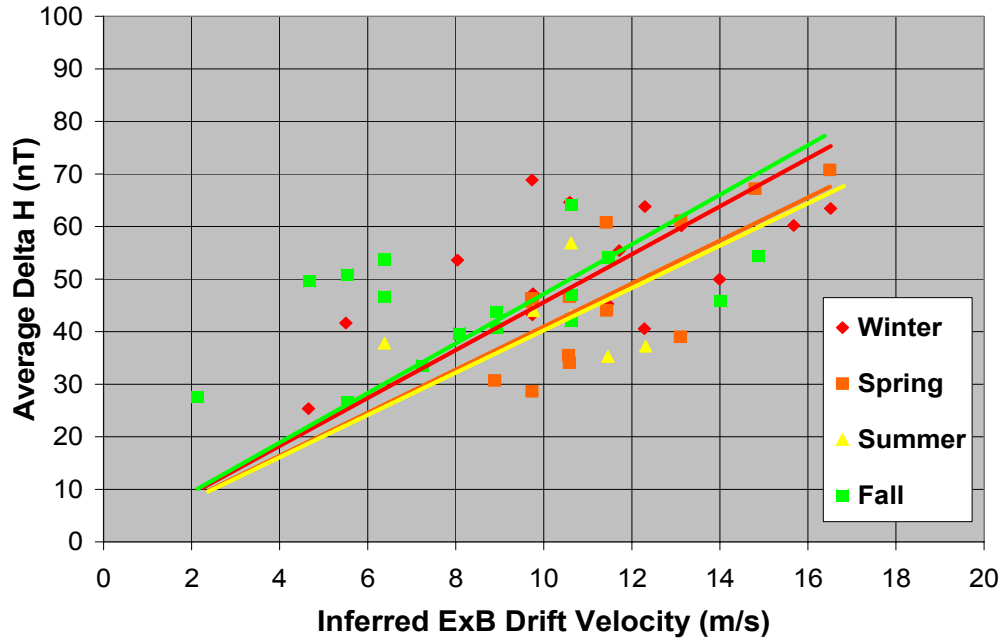


Figure 27. Average ΔH versus Inferred $\vec{E} \times \vec{B}$ Drift Velocity by Season with Points Outside Two Standard Deviations Removed and 0-Offset.

Monthly division seems to be the most appropriate for the Philippine data. In addition to the ascending versus descending data division, maintaining the consistency in the $F_{10.7}$ index provides a more accurate representation of physically similar study days.

However, for the smaller monthly groupings, more data is necessary to improve upon the regressions.

Quiet vs. Disturbed Ascending Days

One final study was conducted on the April (Spring, ascending) data to assess the quality of our regression relation. From the work of many researchers, we know that storm-time high latitude electric fields can “map”, or “penetrate”, toward low magnetic latitudes [Anderson, private communication, 2004]. During magnetic storms, this phenomenon could definitely alter our results by altering the Sq dynamo. Therefore, for

each of the 13 ascending days, the Ap index was determined (24 hour average of the planetary A-index, representing the overall geomagnetic field conditions for a UTC day). By doing so, quiet and disturbed days could be distinguished from each other. Table 12 includes this information:

Table 12. Ap Index, Geomagnetic Conditions, and Regression Data (Ascending Days)

DOY	Ap Index	Conditions	Inferred $\vec{E} \times \vec{B}$ (m/s)	Average ΔH (nT)
91	18.375	Active	10.58	34.078554
94	5.125	Quiet	11.43	44.018885
95	3.250	Quiet	13.10	39.002202
96	3.875	Quiet	9.73	28.625890
98	2.000	Quiet	10.56	35.493788
99	3.125	Quiet	16.50	70.750587
100	5.375	Quiet	9.72	46.332080
101	15.250	Unsettled	10.58	46.643753
102	15.750	Unsettled	11.42	60.801141
103	17.000	Active	9.73	45.657425
106	6.625	Quiet	13.11	61.083832
107	62.000	STORMING	14.80	67.203010
110	70.500	STORMING	8.89	30.688371

[NOAA Satellite and Information Services, 2004]

When the data from April 2002 was plotted again, this time removing the two days of storming, the regression relation did not improve. The relation changed from:

$$\Delta H = 4.9496 (\vec{E} \times \vec{B}) - 10.22 \text{ with } R^2 = 0.6263$$

to

$$\Delta H = 4.4321 (\vec{E} \times \vec{B}) - 4.3696 \text{ with } R^2 = 0.4973$$

Figure 28 illustrates these results. As can be seen by Figure 28, the two storm days do not really represent “outliers” in a statistical sense; in fact, it actually improves the regression when they are included. Possibly with a larger data set, and a larger distribution of quiet versus storming days, this technique may improve the regression.

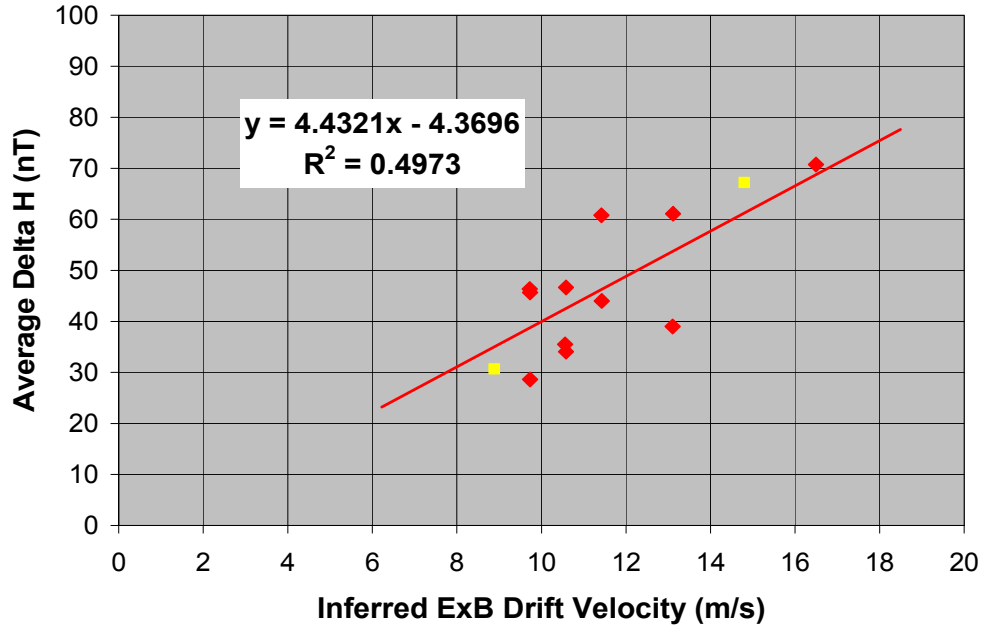


Figure 28. Average ΔH versus Inferred $\vec{E} \times \vec{B}$ Drift Velocity with Quiet and Disturbed Ascending Days Distinguished. The points and trendline in red include ascending days with the two storming days removed. The two yellow points are the removed storming days.

The Final Regression

Because the April 2002 (Spring, ascending) data set provides the most reliable regression relation among any of the techniques attempted, and because it clearly gives the best correlation coefficient, it will be considered the final result of this research.

Again, this final regression is: $\Delta H = 4.9496 (\vec{E} \times \vec{B}) - 10.22$ with an $R^2 = 0.6263$. The 0-offset version of this regression is: $\Delta H = 4.0943 (\vec{E} \times \vec{B})$.

The April 2002 Peruvian result had a 0-offset slope of 4.2784 [Anderson, private communication, 2004]. Applying the earlier argument that ΔH is proportional to $1/B$, we would expect little difference between the slopes; this is shown by the difference of five percent between the Philippine and Peruvian results. On the other hand, taking the

approach that ΔH is proportional to $1/B^2$, the Peruvian result is indeed larger (as predicted by this argument) than the April 2002 result for the Philippines. However, the prediction suggested that there would be a difference in the slopes of 30 percent, based on the magnitude of the geomagnetic field in the two regions. Assuming the physics of this argument is correct, the discrepancy can most likely be attributed to the small size of the ascending data set or the unexplained variance of the latitude crest separation versus $\vec{E} \times \vec{B}$ relation used to infer the drift velocities.

IV. Conclusions and Suggestions for Future Work

This research extended a recent study [Anderson, et al, 2000] to develop a regression relation between vertical $\vec{E} \times \vec{B}$ drifts in the equatorial F-region and the strength of the equatorial electrojet in the Philippine longitude sector. Daytime measurements of the geomagnetic H-component from magnetometer sites in Davao and Muntinlupa were combined to determine daily average values for ΔH , the component of the field due solely to the equatorial electrojet. Using an additional relationship derived by *Anderson* [private communication, 2003], nighttime Global Ultraviolet Imager airglow emission data were then used to estimate the corresponding vertical $\vec{E} \times \vec{B}$ drift velocities. The magnetometer and GUVI data were obtained for 56 days in 2002, however this total data set was regrouped first by satellite orbit type (ascending or descending), and then by the monthly $F_{10.7}$ value. The drift velocities were compared statistically to the values of ΔH for several groupings of data; overall, the best regression relation resulted from the ascending, April 2002 TIMED passes, which included 13 days of data. This result provided a correlation coefficient of 0.63 and was compared to the April 2002 result from the Peruvian sector. In order to do so, our Philippine April regression line was plotted with a 0-offset, resulting in a regression slope of 4.0943. The corresponding Peruvian slope for April 2002 was 4.2784 [Anderson, private communication, 2003].

Based on the previous argument that ΔH is proportional to $1/B$ and the slopes should be relatively equal, the research seems to agree, illustrating only a five percent difference between the Philippine and Peruvian slopes. On the other hand, the Philippine result is also consistent with the $1/B^2$ argument that the Philippine slope should be

smaller than that in Peru. Yet, with only a five percent difference in the slopes, rather than a 30 percent difference as predicted with the $1/B^2$ argument, the $1/B$ argument seems more reasonable. If we could prove that the physical reasoning motivating the $1/B^2$ argument is correct, however, the discrepancy in slopes could be a result of the small sample size of the ascending data set or the 0.60 correlation for the *Anderson* [private communication, 2003] crest separation versus inferred drift relation.

Each regression relation, including the April 2002 result, might also be enhanced through improvements in the *Anderson* [private communication, 2003] relation relating inferred drifts to the anomaly crest separation values. Again, this relationship has a correlation coefficient of 0.60, and was used to calculate every drift velocity used to derive our Philippine regression formulas. Therefore, some level of uncertainty is present in our conclusions. The variance between the actual R^2 value, 0.60, and a perfect R^2 of 1, was not accounted for in this research, but it suggests that the magnitude of the $\vec{E} \times \vec{B}$ drift may depend critically on parameters in addition to the crest separation. Or, a non-linear regression may be necessary to describe this relationship more completely. This argument could also be made for the variance in R^2 for our Philippine ΔH versus $\vec{E} \times \vec{B}$ regression relationships; ΔH may not be the only independent variable or a non-linear approach may be more appropriate.

In addition, the methodology applied throughout the Philippine study could be repeated using Peruvian data and *Anderson's* crest separation versus $\vec{E} \times \vec{B}$ relation instead of observed drifts from the Jicamarca ISR. This would provide some information concerning the validity of this expression and allow an additional comparison with the original Peruvian study.

Maintaining monthly divisions, according to the $F_{10.7}$ index, seems to be the most reliable method for improving upon the remaining regression relations. A much larger database for each of the monthly groupings could facilitate improvement in the correlation coefficients and further comparison could be initiated between the Peruvian and Philippine studies. Also, experience gained throughout the research with the Philippine data suggests that ascending passes (such as the April grouping) result in better statistics than the groups containing only descending passes. Although it is possible that simply increasing the sample size for these additional groupings may improve the relations, there may be inherent differences between ascending and descending passes causing the ascending passes to produce better results. If an inherent difference between ascending and descending passes does exist, this effect might even overwhelm the positive effect of simply adding more data to the study. Additional Peruvian sector studies show that differences in the slopes occur when looking at ascending versus descending orbits as well, yet the sense of this trend is not yet well-defined [Anderson, private communication, 2003].

Unlike the Peruvian results, which could be validated using the Jicamarca Incoherent Scatter Radar (ISR), no data are *currently* available to permit validation of our April 2002 regression relation. However, the Communication/Navigation Outage Forecasting System (C/NOFS) satellite, scheduled for launch in December 2004, will have the ability to measure equatorial electric fields through its vector electric field instrument (VEFI) [AFRL Space Vehicles Directorate, 2004]. When these data are available, it will be possible to validate against inferred drifts calculated via the Philippine ΔH versus $\vec{E} \times \vec{B}$ regression. Also, the Defense Meteorological Satellite

Program/Special Sensor Ultraviolet Spectrographic Imager (DMSP/SSUSI), similar to GUVI, could provide an additional source of empirically-derived electric field values [JHUAPL: SSUSI, 2004]. From a theoretical standpoint, the Scherliess and Fejer climatological model could be used to calculate Philippine region electric fields, and ongoing work by Art Richmond and Astrid Maute at the National Center for Atmospheric Research (NCAR), focused on theoretically calculating $\vec{E} \times \vec{B}$ drifts and corresponding ΔH values, could also be used to validate our observations.

Appendix A: Derivation of the Limiting Form of the Cowling Conductivity

$$\text{Cowling Conductivity} = \sigma_3 = \frac{\sigma_2^2 + \sigma_1^2}{\sigma_1} \quad (\text{A-1})$$

From *Forbes* [1981], we have the following assumptions:

$$\sigma_3 \approx \frac{\sigma_2^2}{\sigma_1} \quad (\text{A-2})$$

$$\omega_e \gg \nu_e \quad (\text{A-3})$$

$$\nu_i \gg \omega_i \quad (\text{A-4})$$

We also know from *Rishbeth and Garriott* [1969]:

$$\sigma_1 = N_e e^2 (k_{le} + k_{li}) \quad (\text{A-5})$$

$$\sigma_2 = N_e e^2 (k_{2e} - k_{2i}) \quad (\text{A-6})$$

$$k_{le} = \frac{1}{Be} \frac{\nu_e \omega_e}{\nu_e^2 + \omega_e^2} \quad (\text{A-7})$$

$$k_{li} = \frac{1}{Be} \frac{\nu_i \omega_i}{\nu_i^2 + \omega_i^2} \quad (\text{A-8})$$

$$k_{2e} = \frac{1}{Be} \frac{\omega_e^2}{\nu_e^2 + \omega_e^2} \quad (\text{A-9})$$

$$k_{2i} = \frac{1}{Be} \frac{\omega_i^2}{\nu_i^2 + \omega_i^2} \quad (\text{A-10})$$

Substituting Equations (A-5) through (A-10) into (A-2), then simplifying, gives:

$$\sigma_3 \approx \frac{N_e e (\nu_i \omega_e - \nu_e \omega_i)^2 (\nu_i \omega_e + \nu_e \omega_i)}{B (\nu_e^2 + \omega_e^2) (\nu_i \nu_e + \omega_i \omega_e) (\nu_i^2 + \omega_i^2)} \quad (\text{A-11})$$

If we now assume (A-3) and (A-4), the terms in Equation (A-11) can be simplified:

$$(\nu_i \omega_e - \nu_e \omega_i)^2 \rightarrow (\nu_i \omega_e)^2 \quad (\text{A-12})$$

$$\nu_i \omega_e + \nu_e \omega_i \rightarrow \nu_i \omega_e \quad (\text{A-13})$$

$$\nu_e^2 + \omega_e^2 \rightarrow \omega_e^2 \quad (\text{A-14})$$

$$\nu_i^2 + \omega_i^2 \rightarrow \nu_i^2 \quad (\text{A-15})$$

Applying (A-12) through (A-15) to Equation (A-11) gives:

$$\sigma_3 \approx \frac{N_e e (\nu_i \omega_e)}{B (\nu_i \nu_e + \omega_i \omega_e)} \quad (\text{A-16})$$

Rishbeth and Garriott [1969] give the following condition, which applies at an altitude of 105 km:

$$\nu_i \nu_e = \omega_i \omega_e \quad (\text{A-17})$$

Using (A-17), Equation (A-16) becomes:

$$\sigma_3 \approx \frac{\nu_i N_e e}{2B \omega_i} \quad (\text{A-18})$$

We know simply:

$$\omega_i = \frac{e B}{m_i} \quad (\text{A-19})$$

Therefore, Equation (A-18) can be rewritten as:

$$\sigma_3 \approx \frac{1}{2} \frac{m_i \nu_i}{B^2} N_e \quad (\text{A-20})$$

$$\approx \frac{m_i \nu_i}{B^2} N_e \quad (\text{A-21})$$

Equation (A-21) is the limiting form from *Forbes* [1981].

Appendix B: IDL Program Source Code

[Anderson and Anghel, private communication, 2003]

```
Pro s2hms_str, second, h,m,s
```

```
  ; Input:  second (of day)
  ; Output: h, m, s  ; hour, minute, second
```

```
  str_name = ['0','1','2','3','4','5','6','7','8','9']
```

```
  h = fix(second/3600.)
  m = fix ((second - h *3600.)/60.)
  s = second - h*3600. - m*60.
  h = fix(h) & m = fix(m) & s= fix(s)
```

```
  h = str_name (h/10) + str_name (h - (h/10) * 10)
  m = str_name (m/10) + str_name (m - (m/10) * 10)
  s = str_name(s/10) + str_name (s - (s/10) * 10)
```

```
  return
end
```

```
;------
; Main program to read data from the GUVI disk file and create test.dat
;------
```

```
GUVI_L1B_data_dir = "
filename = dialog_pickfile(/read, filter= GUVI_L1B_data_dir + '*'+ 'GUVI_im' + '*.L1B')
```

```
;filename = 'test.L1B'
```

```
ID = NCDF_open (filename)
```

```
infor = NCDF_inquire (ID)
```

```
NCDF_VARGET, ID, "DOY",          doy
NCDF_VARGET, ID, "Time",        time
NCDF_VARGET, ID, "Detector",     detector
NCDF_VARGET, ID, "MirrorNadirPosition", nadir
NCDF_VARGET, ID, "RadianceData", radiance
NCDF_VARGET, ID, "PiercePointLatitude", lat
NCDF_VARGET, ID, "PiercePointLongitude", lon
NCDF_VARGET, ID, "CountError",   CountErr
```

```

NCDF_VARGET, ID, "DQI",          dqI
NCDF_VARGET, ID, "CalibrationError", CalErr

NCDF_CLOSE, ID

OPENW, 1, 'Err_test291.dat

n_scans = n_elements (time)
second = time/1000.

PRINTF, 1, FORMAT = '("No. DOY Hr:Mn:Sc  Radiance1  Radiance2  Radiance3
Radiance4  RadianceT  Lat1   Lat2   Lat3   Lat4   LatT   Long1   Long2
Long3   Long4   LongT")'

for k = 0, n_scans-1 do begin
    current_scan = strcompress(string(fix(k+1)))
    s2hms_str, second(k), h_name, m_name, s_name
    current_time = h_name + ':' + m_name + ':' + s_name

    sumlat = 0.0
    sumlon = 0.0
    count = 0
    for i = 0, 13 do begin
        for j = 0, 39 do begin
            sumlat = sumlat + lat(i,j,k)
            sumlon = sumlon + lon(i,j,k)
            count = count + 1
        endfor
    endfor

    lat1 = sumlat/count
    lon1 = sumlon/count

    sum = 0.0
    count = 0.0
    for i = 0, 13 do begin
        for j = 0, 39 do begin
            if (radiance (2,i,j,k) NE 0.0) AND $
                (    dqI(2,i,j,k) EQ 0.0 ) AND $
                ( counter(2,i,j,k) LT 2000.0 ) then begin
                sum = sum + radiance(2,i,j,k)
                count = count + 1
            endif
        endfor
    endfor
endfor

```

```

if ( count NE 0 ) then begin
    radiance1 = sum/count
    ;print, count
endif else begin
    radiance1 = 0.0
endelse

sumlat = 0.0
sumlon = 0.0
count = 0
for i = 0, 13 do begin
    for j = 40, 79 do begin
        sumlat = sumlat + lat(i,j,k)
        sumlon = sumlon + lon(i,j,k)
        count = count + 1
    endfor
endfor

lat2 = sumlat/count
lon2 = sumlon/count

sum = 0.0
count = 0.0
for i = 0, 13 do begin
    for j = 40, 79 do begin
        if ( radiance(2,i,j,k) NE 0.0 ) AND $
            ( dqi(2,i,j,k) EQ 0.0 ) AND $
            ( counterr(2,i,j,k) LT 2000.0 ) then begin
            sum = sum + radiance(2,i,j,k)
            count = count + 1
        endif
    endfor
endfor

if ( count NE 0 ) then begin
    radiance2 = sum/count
    ;print, count
endif else begin
    radiance2 = 0.0
endelse

sumlat = 0.0
sumlon = 0.0
count = 0
for i = 0, 13 do begin

```

```

    for j = 80, 119 do begin
        sumlat = sumlat + lat(i,j,k)
        sumlon = sumlon + lon(i,j,k)
        count = count + 1
    endfor
endfor

lat3 = sumlat/count
lon3 = sumlon/count

sum = 0.0
count = 0.0
for i = 0, 13 do begin
    for j = 80, 119 do begin
        if ( radiance(2,i,j,k) NE 0.0 ) AND $
            ( dqi(2,i,j,k) EQ 0.0 ) AND $
            ( counterr(2,i,j,k) LT 2000.0 ) then begin
            sum = sum + radiance(2,i,j,k)
            count = count + 1
        endif
    endfor
endfor

if ( count NE 0 ) then begin
    radiance3 = sum/count
    ;print, count
endif else begin
    radiance3 = 0.0
endelse

sumlat = 0.0
sumlon = 0.0
count = 0
for i = 0, 13 do begin
    for j = 120, 158 do begin
        sumlat = sumlat + lat(i,j,k)
        sumlon = sumlon + lon(i,j,k)
        count = count + 1
    endfor
endfor

lat4 = sumlat/count
lon4 = sumlon/count

sum = 0.0

```

```

count = 0.0
for i = 0, 13 do begin
  for j = 120, 158 do begin
    if ( radiance(2,i,j,k) NE 0.0 ) AND $
      ( dqi(2,i,j,k) EQ 0.0 ) AND $
      ( counterr(2,i,j,k) LT 2000.0 ) then begin
      sum = sum + radiance(2,i,j,k)
      count = count + 1
    endif
  endfor
endfor

```

```

if ( count NE 0 ) then begin
  radiance4 = sum/count
  ;print, count
endif else begin
  radiance4 = 0.0
endelse

```

```

sumlat = 0.0
sumlon = 0.0
count = 0
for i = 0, 13 do begin
  for j = 0, 158 do begin
    sumlat = sumlat + lat(i,j,k)
    sumlon = sumlon + lon(i,j,k)
    count = count + 1
  endfor
endfor

```

```

latT = sumlat/count
lonT = sumlon/count

```

```

sum = 0.0
count = 0.0
for i = 0, 13 do begin
  for j = 0, 158 do begin
    if ( radiance(2,i,j,k) NE 0.0 ) AND $
      ( dqi(2,i,j,k) EQ 0.0 ) AND $
      ( counterr(2,i,j,k) LT 2000.0 ) then begin
      sum = sum + radiance(2,i,j,k)
      count = count + 1
    endif
  endfor
endfor

```

```

if ( count NE 0 ) then begin
    radianceT = sum/count
    ;print, count
endif else begin
    radianceT = 0.0
endelse

if (( lat1 GT -40.0 ) AND ( lat1 LT 40.0 )) OR $
(( lat2 GT -40.0 ) AND ( lat2 LT 40.0 )) OR $
(( lat3 GT -40.0 ) AND ( lat3 LT 40.0 )) OR $
(( lat4 GT -40.0 ) AND ( lat4 LT 40.0 )) then begin

    if(( lon1 GT 100.0 ) AND ( lon1 LT 140.0 )) OR $
    (( lon2 GT 100.0 ) AND ( lon2 LT 140.0 )) OR $
    (( lon3 GT 100.0 ) AND ( lon3 LT 140.0 )) OR $
    (( lon4 GT 100.0 ) AND ( lon4 LT 140.0 )) then begin

        ;if ( latT GT -40.0 ) AND ( latT LT 40.0 ) AND ( lonT GT 100.0 ) AND ( lonT LT
140.0 ) then begin
            PRINTF, 1, FORMAT = '(% "%3d %3d %s %8.2f %8.2f %8.2f %8.2f %8.2f
%7.2f %7.2f %7.2f %7.2f %7.2f %8.2f %8.2f %8.2f %8.2f %8.2f")', $
                current_scan, doy(k), current_time, radiance1, radiance2, radiance3,
radiance4, radianceT, lat1, lat2, lat3, lat4, latT, lon1, lon2, lon3, lon4, lonT
            endif
        endif

        print, 'k = ', k

    endfor

    CLOSE, 1

    END

```

Bibliography

- AFRL Space Vehicles Directorate. "The Communication/Navigation Outage Forecasting System (C/NOFS)" n. pag. <http://www.vs.afrl.af.mil/TechProgs/CNOFS/>. (4 May 2004).
- AFSPC/DORW. "Space Environmental Impacts on DoD Operations," *FYI*, No. 37, Air Weather Service, Peterson AFB, CO (February 1997).
- Anderson, D., A. Anghel, K. Yumoto, M. Ishitsuka, and E. Kudeki. "Estimating Daytime Vertical $\vec{E} \times \vec{B}$ Drift Velocities in the Equatorial F-Region Using Ground-Based Magnetometer Observations," *Geophysical Research Letters*. Vol. 29, No. 12, p. 37(1)-37(4), 2002.
- Johns Hopkins University Applied Physics Laboratory, The. "GUVI: Global Ultraviolet Imager." n. pag. <http://guvi.jhuapl.edu/home.html>. (4 September 2003).
- Johns Hopkins University Applied Physics Laboratory, The. "SSUSI: Horizon-to-Horizon and Limb-Viewing Spectrographic Imager for Remote Sensing of Environmental Parameters," n. pag. http://guvi.jhuapl.edu/documents/msword/huffman_spie_revised/huffman_spie_revised.html. (4 May 2004).
- Johns Hopkins University Applied Physics Laboratory, The. "TIMED: A Mission to Explore One of the Last Frontiers in Earth's Atmosphere," n. pag. <http://www.timed.jhuapl.edu/>. (27 August 2003).
- Kelley, M.C. *The Earth's Ionosphere: Plasma Physics and Electrodynamics*. San Diego: Academic Press, Inc., 1989.
- Knecht, D.J., and B. M. Shuman. "The Geomagnetic Field," in *Handbook of Geophysics and the Space Environment*. Ed. A.S. Jursa. p. 4-2, Air Force Geophysics Laboratory, 1985.
- Kyushu University, Space and Earth Electromagnetism Laboratory. "The Circum-Pacific Magnetometer Network: Stations List (1995) and Maps," n. pag. <http://denji102.geo.kyushu-u.ac.jp/denji/obs/cpmn/station/STAT95.htm>. (4 August 2003).
- NOAA Satellite and Information Services. "Space Physics Interactive Data Resource," n. pag. <http://spidr.ngdc.noaa.gov/spidr/>. (21 April 2004).
- NOAA Space Environment Center. "Recent Solar Indices," n. pag. <http://www.sec.noaa.gov/ftplib/weekly/RecentIndices.txt>. (14 January 2004)

- Rastogi, R.G. "The Equatorial Electrojet: Magnetic and Ionospheric Effects," in *Geomagnetism*. Ed. J.A. Jacobs. Vol. 3, p. 461-525, Academic Press, 1989.
- Rees, M.H. *Physics and Chemistry of the Upper Atmosphere*. Cambridge: Cambridge University Press, 1989.
- Richmond, A.D. "Equatorial Electrojet - I. Development of a Model Including Winds and Instabilities," *Journal of Atmospheric and Terrestrial Physics*. Vol. 35, p. 1083-1103, 1973.
- Rishbeth, H., and O.K. Garriott. *Introduction to Ionospheric Physics*. New York: Academic Press, 1969.
- Scherliess, L., and B.G. Fejer. "Radar and Satellite Global Equatorial F-Region Vertical Drift Model," *Journal of Geophysical Research*. Vol. 104, No. A4, p. 6829-6842, 1999.
- Schunk, R.W., and A.F. Nagy. *Ionospheres: Physics, Plasma Physics, and Chemistry*. New York: Cambridge University Press, 2000.
- Schunk, R.W., L. Scherliess, J.J. Sojka, D.C. Thompson, D.N. Anderson, M. Codrescu, C. Minter, T.J Fuller-Rowell, R.A Heelis, M. Hairston, and B.M. Howe, "Global Assimilation of Ionospheric Measurements (GAIM)," *Radio Science*, Vol. 39, No. 1 (January 2004).
- Tascione, T. F. *Introduction to the Space Environment* (2nd Edition). Malabar FL: Krieger Publishing Co., 1994.
- Volland, H. *Atmospheric Electrodynamics*. Berlin: Springer-Verlag, 1984.
- West, K.H. and R.A. Heelis. "Longitude Variations in Ion Composition in the Morning and Evening Topside Equatorial Ionosphere Near Solar Minimum," *Journal of Geophysical Research*. Vol. 101, No. A4, p. 7951-7960, 1996.
- Yumoto, K. "Characteristics of Pi 2 Magnetic Pulsations Observed at the CPMN Stations: A Review of the STEP Results," *Earth, Planets, and Space*. Vol. 53, p. 981-992, 2001.

Vita

Ms. Shauna Kinkela was born and raised in Pennsylvania, where she graduated, with high honors, from Penn Trafford High School. She attended Saint Vincent College in Latrobe, Pennsylvania, where she graduated with high honors and earned a Bachelor of Science degree in Physics with a minor in Mathematics. Ms. Kinkela began her graduate education at the Air Force Institute of Technology to pursue a Masters of Science degree in Applied Physics (Space Weather). Upon graduation, she will begin working as a UCAR Visiting Scientist for the Air Force Weather Agency, Offutt AFB, Nebraska.

REPORT DOCUMENTATION PAGE				Form Approved OMB No. 074-0188	
<p>The public reporting burden for this collection of information is estimated to average 1 hour per response, including the time for reviewing instructions, searching existing data sources, gathering and maintaining the data needed, and completing and reviewing the collection of information. Send comments regarding this burden estimate or any other aspect of the collection of information, including suggestions for reducing this burden to Department of Defense, Washington Headquarters Services, Directorate for Information Operations and Reports (0704-0188), 1215 Jefferson Davis Highway, Suite 1204, Arlington, VA 22202-4302. Respondents should be aware that notwithstanding any other provision of law, no person shall be subject to a penalty for failing to comply with a collection of information if it does not display a currently valid OMB control number.</p> <p>PLEASE DO NOT RETURN YOUR FORM TO THE ABOVE ADDRESS.</p>					
1. REPORT DATE (DD-MM-YYYY) June 2004		2. REPORT TYPE Master's Thesis		3. DATES COVERED (From – To) June 2003-May 2004	
4. TITLE AND SUBTITLE ESTIMATING EQUATORIAL F-REGION DAYTIME VERTICAL $\vec{E} \times \vec{B}$ DRIFT VELOCITIES FROM GROUND-BASED MAGNETOMETER MEASUREMENTS IN THE PHILIPPINE LONGITUDE SECTOR				5a. CONTRACT NUMBER	
				5b. GRANT NUMBER	
				5c. PROGRAM ELEMENT NUMBER	
				5d. PROJECT NUMBER	
6. AUTHOR(S) Kinkela, Shauna M., Civilian				5e. TASK NUMBER	
				5f. WORK UNIT NUMBER	
7. PERFORMING ORGANIZATION NAMES(S) AND ADDRESS(S) Air Force Institute of Technology Graduate School of Engineering and Management (AFIT/EN) 2950 Hobson Way, Building 640 WPAFB OH 45433-7765				8. PERFORMING ORGANIZATION REPORT NUMBER AFIT/GAP/ENP/04-04	
9. SPONSORING/MONITORING AGENCY NAME(S) AND ADDRESS(ES) HQ AFWA/DNX Offutt AFB, NE 68113				10. SPONSOR/MONITOR'S ACRONYM(S)	
				11. SPONSOR/MONITOR'S REPORT NUMBER(S)	
12. DISTRIBUTION/AVAILABILITY STATEMENT APPROVED FOR PUBLIC RELEASE; DISTRIBUTION UNLIMITED					
13. SUPPLEMENTARY NOTES					
14. ABSTRACT <p>Ionospheric disturbances can severely impact Department of Defense (DoD) systems, such as radar, satellite, and navigation technologies. Forecasting disturbances and describing the Earth's ionosphere, in turn, relies upon innovative computer-based models that gather input parameters from ground and space-borne observations and empirical models for ionospheric drivers. Equatorial $\vec{E} \times \vec{B}$ drift velocities are significant input parameters that go into many ionospheric models, because they help describe vertical plasma motions near the magnetic equator. Previous work by <i>Anderson, et al</i> [2002] has demonstrated the ability to derive Peruvian longitude sector, daytime vertical $\vec{E} \times \vec{B}$ drifts from ground-based magnetometer data. The present research extends these results to the Philippines using 56 days of magnetometer data from two stations in 2002. For each day of magnetometer data, corresponding Global Ultraviolet Imager (GUVI) 1356Å airglow emission data from the evening equatorial anomaly were used to estimate the average $\vec{E} \times \vec{B}$ drift velocities [Anderson, private communication, 2003]. These drift values were then compared statistically to the horizontal component of the Philippine magnetometer data for all 56 days. In this process, data were grouped according to $F_{10.7}$ values. Overall, the best regression relation resulted from the ascending, April 2002 sample of 13 days of data (correlation coefficient of 0.63). Previous research does not conclusively predict how our April 2002 Philippine slope should compare against the corresponding Peruvian result. Specifically, <i>Richmond</i> [1973] predicts the two slopes should be approximately equal. However, <i>Forbes</i> [1981] suggests the Philippine regression slope should be 30 percent smaller than the corresponding Peruvian slope. Our calculated slope difference between the two regression relations is five percent, leaning more toward <i>Richmond's</i> prediction. However, we must keep in mind that our crest separation versus $\vec{E} \times \vec{B}$ relation has a correlation of 0.6, leaving 40 percent of unaccounted variance. Unlike <i>Anderson's</i> Peruvian results, no data currently exist to permit validation of our regression relation, yet C/NOFS electric field measurements, when available, may help settle the issue.</p>					
15. SUBJECT TERMS Ionosphere, electrodynamic drift, equatorial electrojet, equatorial anomaly, magnetometer, GUVI					
16. SECURITY CLASSIFICATION OF:			17. LIMITATION OF ABSTRACT UU	18. NUMBER OF PAGES 99	19a. NAME OF RESPONSIBLE PERSON Devin J. Della-Rose, Major, USAF (ENP)
REPORT U	ABSTRACT U	c. THIS PAGE U			19b. TELEPHONE NUMBER (Include area code) (937) 255-3636, ext 4514 e-mail: Devin.Della-Rose@afit.edu